Article

Neuron

A Combination of Ontogeny and CNS Environment Establishes Microglial Identity

Graphical Abstract

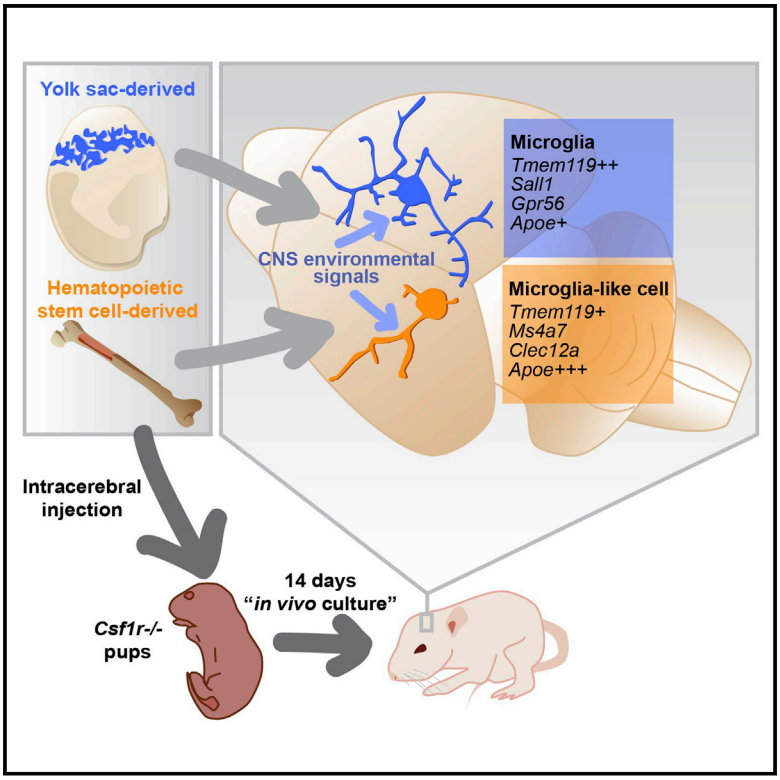

Authors

F. Chris Bennett, Mariko L. Bennett, Fazeela Yaqoob, ..., Melanie Hayden Gephart, Edward D. Plowey, Ben A. Barres

Correspondence

eph.bennett@gmail.com

In Brief

Bennett et al. create a macrophage transplantation system to measure how origin and brain environment contribute to microglial identity. Although diverse macrophage types survive in the brain, only those sharing developmental origins with microglia express microglial genes normally.

Highlights

- Brain signals induce and sustain homeostatic gene expression in microglia
- Hematopoietic stem cell (HSC)-derived macrophages attain a microglia-like identity
- Stable markers and gene signatures betray HSC origin
- Macrophages with HSC origin markers are found in human neurodegeneration

Bennett et al., 2018, Neuron *98*, 1170–1183
June 27, 2018
https://doi.org/10.1016/j.neuron.2018.05.014

CellPress

CellPress

Neuron
Article

A Combination of Ontogeny and CNS Environment Establishes Microglial Identity

F. Chris Bennett,[1,2,5,*] Mariko L. Bennett,[1] Fazeela Yaqoob,[1] Sara B. Mulinyawe,[1] Gerald A. Grant,[3] Melanie Hayden Gephart,[3] Edward D. Plowey,[4] and Ben A. Barres[1]
[1]Department of Neurobiology, Stanford University School of Medicine, Stanford, CA 94305, USA
[2]Department of Psychiatry and Behavioral Sciences, Stanford University School of Medicine, Stanford, CA 94305, USA
[3]Department of Neurosurgery, Stanford University School of Medicine, Stanford, CA 94305, USA
[4]Department of Pathology, Stanford University School of Medicine, Stanford, CA 94305, USA
[5]Lead Contact
*Correspondence: eph.bennett@gmail.com
https://doi.org/10.1016/j.neuron.2018.05.014

SUMMARY

Microglia, the brain's resident macrophages, are dynamic CNS custodians with surprising origins in the extra-embryonic yolk sac. The consequences of their distinct ontogeny are unknown but critical to understanding and treating brain diseases. We created a brain macrophage transplantation system to disentangle how environment and ontogeny specify microglial identity. We find that donor cells extensively engraft in the CNS of microglia-deficient mice, and even after exposure to a cell culture environment, microglia fully regain their identity when returned to the CNS. Though transplanted macrophages from multiple tissues can express microglial genes in the brain, only those of yolk-sac origin fully attain microglial identity. Transplanted macrophages of inappropriate origin, including primary human cells in a humanized host, express disease-associated genes and specific ontogeny markers. Through brain macrophage transplantation, we discover new principles of microglial identity that have broad applications to the study of disease and development of myeloid cell therapies.

INTRODUCTION

Microglia are vital residents of the brain parenchyma, where they play important but poorly understood roles in development, injury, and disease (Li and Barres, 2018; Salter and Stevens, 2017). Arising from yolk sac erythro-myeloid progenitors (YS EMPs) that colonize neural tissue during embryogenesis and undergo a distinct maturational process, microglia are unique among tissue macrophages in that they are thought to remain YS derived throughout life, without contribution from the fetal liver or definitive hematopoiesis (Ginhoux et al., 2010; Hagemeyer et al., 2016; Hoeffel et al., 2015; Kierdorf et al., 2013; Gomez Perdiguero et al., 2015; Schulz et al., 2012). After insults such as experimental autoimmune encephalomyelitis, stroke, malignancy, or genetic depletion, however, microglia dramatically change their phenotype and are joined by infiltrating monocytes/macrophages from the circulation (Ajami et al., 2011; Varvel et al., 2012). These CNS-alien, hematopoietic stem cell (HSC)-derived occupants can resemble microglia in morphology and surface marker expression but appear to participate differently in disease pathogenesis, making it essential to further clarify their functions. Identification of a microglia-specific gene cassette has improved resolution of resident from infiltrating cells (Bennett et al., 2016; Hickman et al., 2013), but does not address whether infiltrating cells inherently lack the capacity to become microglia under appropriate conditions, nor whether microglia can irreversibly lose their identity in abnormal environments.

Although circulating monocytes can effectively differentiate into tissue macrophages in the lung and liver (Scott et al., 2016; van de Laar et al., 2016), the CNS environment is highly distinct and protected from exposure to circulating factors and cells by the blood-brain barrier (BBB) (Obermeier et al., 2013). As such, the precise contributions of ontogeny and CNS environment, which have been highly implicated in microglial identity (Gosselin et al., 2014; Lavin et al., 2014; Mass et al., 2016), remain incompletely understood. Do microglia permanently change their identity following disease, or can they return to a homeostatic state? Like YS-derived cells, can macrophages derived from HSCs become microglia? The answers are critical not only to how microglia and infiltrating myeloid cells affect the brain, but also to the growing use of myeloid cell therapies such as HSC transplantation to treat brain disease in humans (Biffi et al., 2013).

Since our goal was to precisely measure how ontogeny and environment affect microglial identity, we aimed to create a system for transplantation of myeloid cells across development into the brain. We took advantage of *Csf1r*$^{-/-}$ mice, which lack microglia (Dai et al., 2002; Ginhoux et al., 2010; Liddelow et al., 2017), and found that directly injected myeloid cells extensively engraft in the brain parenchyma, allowing study of donor populations with varied ontogeny. Transplantation into *Csf1r*$^{-/-}$ hosts offers several advantages. It can be used to study donor cells of diverse origin and developmental stage, and does not require conditioning irradiation or chemotherapy. It yields large numbers of donor-derived microglia-like cells (MLCs) that have been

conditioned by the brain parenchyma to express microglial genes in the absence of potentially confounding host macrophages, overcoming limitations of prior foundational approaches to understanding microglial identity (Bennett et al., 2016; Bruttger et al., 2015; Mildner et al., 2007).

By comparing multiple engrafted microglia types to MLCs from YS and HSC lineages, we found that microglial identity remains intact *ex vivo*, even following cell culture. We noted general similarity between MLCs derived from all donor lineages, but found striking ontogeny-dependent differences between HSC- and YS-derived populations, leading to discovery of durable markers of parenchymal macrophage ontogeny. We extended this approach to a humanized transplantation system and verified fundamental conclusions in human microglia and MLCs. In sum, we devised an experimental system to unravel the contributions of brain environment and ontogeny to macrophage identity in mouse and human.

RESULTS

Directly Transplanted Microglia Engraft and Ramify in the *Csf1r*$^{-/-}$ CNS

We recently demonstrated that cultured microglia have the capacity to engraft in the *Csf1r*$^{-/-}$ brain parenchyma, which otherwise lacks microglia, after intracerebral transplantation (ICT) (Bohlen et al., 2017). To further study intrinsic versus acquired properties of microglial identity, we compared three distinct microglia populations after ICT into the CNS between postnatal day 0 and 4 (P0–P4): (1) acutely isolated mature microglia (P21, ICT MG); (2) developmentally immature microglia (P5, ICT P5 MG), which lack expression of the full microglial gene cassette (Bennett et al., 2016); and (3) cultured microglia (P18–P35, ICT Cultured MG), which undergo dramatic transcriptional changes *in vitro* including loss of expression of the microglial signature cassette (Bohlen et al., 2017; Gosselin et al., 2017) (Figure 1A). By 14 days after intracerebral injection, all donor microglia types extensively engrafted and ramified in the brain parenchyma, often filling entire sagittal sections (Figures 1B and S1A). When normalized to area of engraftment, transplanted microglia reached a similar density to endogenous microglia in a wild-type *Csf1r*$^{+/+}$ (WT) host (Figure S1B). By flow cytometric analysis, engrafted cells were CD45+CD11B+ and expressed WT levels of TMEM119 (Figures S1C–S1E). By immunostaining, 100% were TMEM119+ in sections from 4–7 biological and at least 5 technical replicates each across the brain. As in WT mice, we found no TMEM119 staining in the meninges and choroid plexus of ICT mice (data not shown). Extent of donor cell engraftment varied—by fluorescence-activated cell sorting (FACS), we retrieved fewer microglia from transplanted hosts than WT controls and occasionally observed minimal to no engraftment. Because the host strain for *Csf1r*$^{-/-}$ transplant experiments was FVB, for which no robustly expressed fluorescent reporters exist, we also verified that sorted engrafted microglia were WT at the *Csf1r* locus (Figure S1F). These data show that microglia from multiple developmental stages can occupy the postnatal brain, ramify, and express TMEM119 only when engrafted in the parenchyma.

CNS Signals Are Sufficient to Induce, Sustain, and Re-induce Microglial Identity

To better understand relationships between microglial ontogeny, environment, and transcriptional phenotype, we used optimized techniques to isolate RNA from highly pure parenchymal microglia after ICT into *Csf1r*$^{-/-}$ hosts based on TMEM119 immunoreactivity (Bennett et al., 2016). Transcriptomic profiling by RNA sequencing (RNA-seq) showed that by 14 days *in vivo*, microglia that had either lost expression of signature genes *in vitro* (ICT Cultured MG) or not attained full maturity (ICT P5 MG) expressed mature microglial signature genes at nearly normal levels, including *Tmem119*, *P2ry12*, *Olfml3*, and *Sall1* (Figure 1C). More broadly, ICT cultured, P5, and adult microglia were highly similar to each other and to their WT counterparts. Of 1,827 differentially expressed genes in *in vitro* microglia, all but 16 returned to within 2-fold of WT levels after re-engraftment of cultured microglia in the CNS (Figure S1G). Volcano plot overlays demonstrate that differences between cultured WT microglia are largely restored after re-engraftment in the brain (Figure 1D). While transplanted microglia have statistically meaningful differences in gene expression compared to untransplanted WT microglia, these changes likely represent an "engraftment signature" from donor cell isolation, culture, and the *Csf1r*$^{-/-}$ host environment. Gene expression changes were generally of small magnitude and included several chemokines, tetraspanins, and G protein-coupled receptors, but not a signature of reactivity or specific functional process (Table S1). These experiments show that the *Csf1r*$^{-/-}$ CNS is sufficient to sustain, induce, and re-induce microglial identity, and that microglial identity potential persists despite dramatic transcriptional perturbations induced *ex vivo*.

Transplanted Cells of Diverse Ontogeny Engraft and Ramify in the *Csf1r*$^{-/-}$ CNS

Given stable microglial identity despite highly plastic gene expression between adult, P5, and cultured microglia, we appreciated that ICT could clarify relationships between brain macrophage ontogeny and environment. In particular, we wondered whether HSC- or YS-derived macrophages originating outside the developed brain could become microglia in a permissive CNS environment capable of supporting homeostatic microglia. Therefore, we individually transplanted whole tissues and sorted myeloid cells into the *Csf1r*$^{-/-}$ CNS at P0–P4, including YS-derived cells from yolk sac and fetal brain, HSC-derived cells from blood and bone marrow (BM), and monocytes from the fetal liver, which, at embryonic day 13 (E13)–E14, contains a mix of HSC- and YS-derived cells (Hoeffel et al., 2015; Gomez Perdiguero et al., 2015). We observed extensive engraftment of ramified IBA1+/TMEM119+ MLCs using all tissue types tested across both embryonic and postnatal lineages (Figures 2A, 2B, S2A–S2C, and S2F), though YS-derived MLCs (YS-MLCs) had a consistently more ramified morphology than HSC-derived MLCs (HSC-MLCs). We verified donor origin of MLCs using a GFP reporter after backcrossing the *Csf1r*$^{-/-}$ allele to C57BL/6 (Figure 2B), and additionally noted extensive coverage of the spinal cord by donor cells delivered by supratentorial injection (Figure S2D).

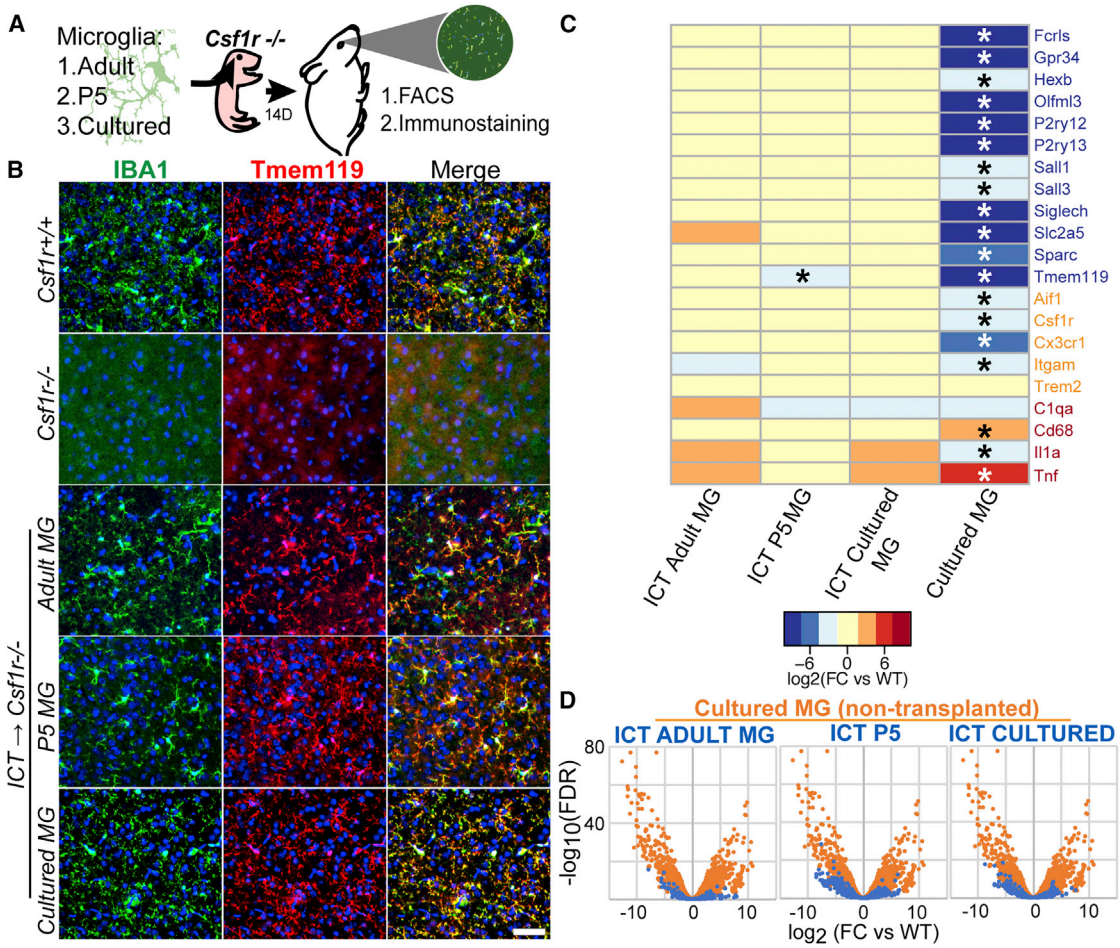

Figure 1. Transplanted Microglia Engraft in the *Csf1r*$^{-/-}$ Brain and Express Tmem119

(A) Schematic of microglial transplantation system.

(B) Immunostaining showing ramified IBA1+(green)/TMEM119+(red) microglia in *Csf1r*$^{+/+}$ (WT) and microglia-transplanted *Csf1r*$^{-/-}$ hosts, and untransplanted *Csf1r*$^{-/-}$ control. Scale bar, 50 μm.

(C) Expression heatmap (log_2(FC/WT)) of microglia (blue), myeloid (orange), and reactivity (red) genes by microglia after culture or transplantation into *Csf1r*$^{-/-}$ CNS. Detailed inventory of experimental replicates is listed in methods. *FDR < 0.05 compared with WT.

(D) Overlaid volcano plots show reduced differential gene expression of ICT cells (blue) compared to non-transplanted cultured microglia (orange), represented by reduced spread of volcano.

See also Figure S1.

By flow cytometry, nearly all CD45+CD11B+ cells were TMEM119 immunoreactive, although HSC donor tissues consistently showed lower intensity staining than WT (Figure 2C). Since we saw a small TMEM119-negative population in some cases, we again confirmed by immunostaining that, as with transplanted microglia, all parenchymal but no other IBA1+ MLCs were TMEM119+ (Figure S2G). All donor tissues engrafted to similar densities as microglia in *Csf1r*$^{-/-}$ brains, except for fetal liver, which reached a significantly higher density (Figure S2E). FACS plots, engraftment levels, and percent TMEM119-positive values are further detailed in Figure S2 to provide potential users a realistic assessment of the robustness of this system.

An inherent limitation of the *Csf1r*$^{-/-}$ model is poor host viability, which required us to measure the effects of CNS residence in ICT experiments after 14 days. To better study the trajectory of effects of longer incubation, we also created a chemotherapy- and irradiation-free peripheral BM transplantation system that allows study of long-term MLC engraftment. Whereas *Csf1r*$^{-/-}$ mice do not typically survive past weaning age (Dai et al., 2002; Li et al., 2006), simple intraperitoneal (i.p.) injection of WT BM "rescued" approximately 50% of pups, leading to prolonged survival, tooth eruption, occasional fertility, and engraftment of donor-derived myeloid cells in multiple tissues including the brain parenchyma and liver (Figures 3A–3D, S3A, and S3B). By 1 month, the brain parenchyma of rescued mice showed complete, uniform coverage by donor-derived cells (Figure 3A). We harvested well-appearing rescued mice up to 1 year after transplantation and observed stable occupancy of the brain parenchyma by MLCs (Figure 3B). Taken together, these studies

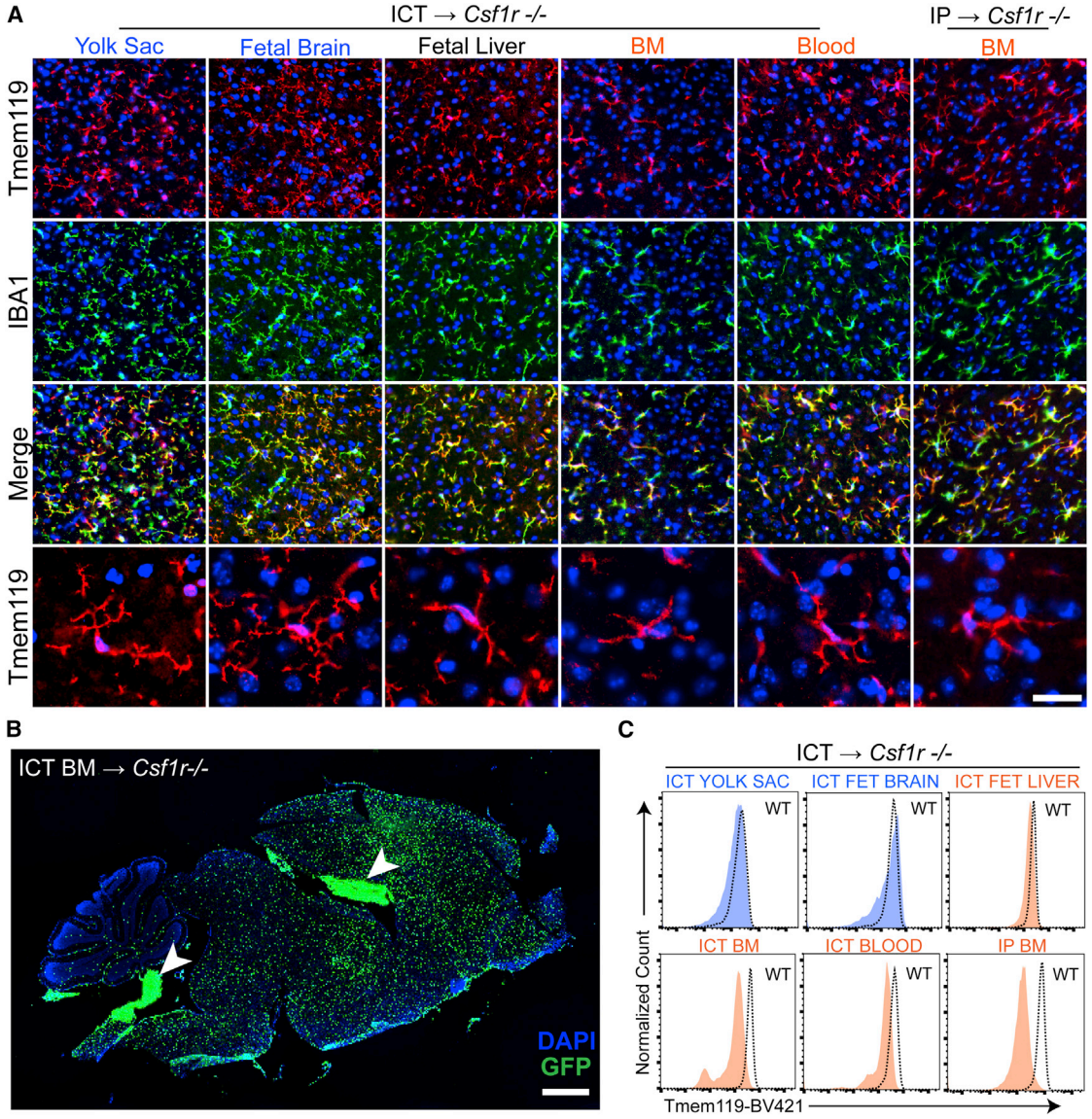

Figure 2. Diverse Myeloid Populations Engraft in the *Csf1r*$^{-/-}$ Brain, Ramify, and Are Tmem119+

(A) IBA1+ (green) MLCs ramify and are TMEM119+ (red) in the brain parenchyma 14 days after ICT into *Csf1r*$^{-/-}$ hosts. Bottom row depicts TMEM119+ MLCs at high magnification. Scale bar, 36.5 μm (top 3 rows), 25 μm (bottom row).

(B) Engrafted GFP+ MLCs 14 days after BM ICT into P1 *Csf1r*$^{-/-}$ host. Arrowheads indicate non-parenchymal donor cells in the ventricles and choroid plexus, of which virtually all are IBA1 positive (Figure S2F). Scale bar, 900 μm.

(C) Histograms show TMEM119 expression in MLCs by flow cytometry 14 days after transplantation, including reduced staining in HSC-MLCs.

See also Figure S2.

show that the CNS niche readily hosts macrophages from multiple donor tissues, including for long periods using BM.

The surprising observation that intraperitoneally injected BM populated the *Csf1r*$^{-/-}$ brain without preconditioning led us to further characterize how donor cells might enter the brain. Since a prior study of macrophage repopulation by peripheral cells found evidence for increased BBB permeability (Varvel et al., 2012), we tested for the presence of increased levels of IgG and albumin in the brain, which are largely excluded from the parenchyma under homeostatic conditions. Quantitative region of interest (ROI) analysis of immunostained histological sections showed no evidence for increased albumin or IgG extravasation, and we did not observe focal areas of increased staining, suggesting "normal" BBB permeability (Figure S3C). Since multiple studies suggest that monocyte infiltration into the diseased or injured CNS is facilitated by CCR2 (Ajami et al., 2011; Dzenko et al., 2001), we wondered whether engraftment of MLCs was similarly CCR2 dependent in *Csf1r*$^{-/-}$ hosts. We found that, as with WT BM, i.p. injection of CCR2 *Rfp/Rfp* (*Ccr2* knockout) BM (Saederup et al.,

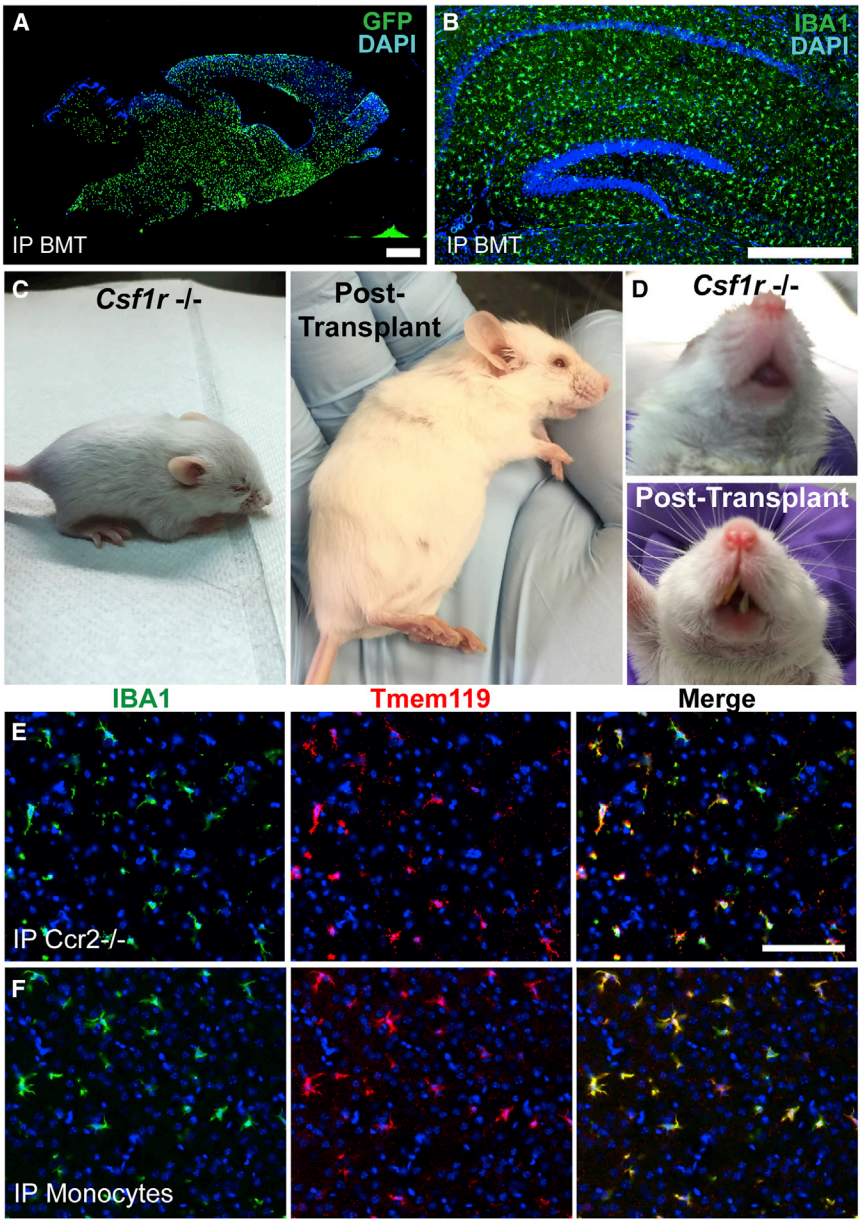

Figure 3. Peripheral BM Injection Leads to Widespread Engraftment of Donor-Derived Cells and Results in Partial Rescue of the *Csf1r*$^{-/-}$ Phenotype; Both Purified Monocytes and *Ccr2*$^{-/-}$ BM Cells Engraft in the *Csf1r*$^{-/-}$ Brain and Express Tmem119

(A) Engrafted MLCs 1 month after i.p. BM injection into P1 host. Scale bar, 900 μm.

(B) Hippocampal section of *Csf1r*$^{-/-}$ brain stained for IBA1 8 months after i.p. BMT. Scale bar, 400 μm.

(C) Typical *Csf1r*$^{-/-}$ mouse showing abnormal head shape and small size (left), compared to 3 months after i.p. BM injection at P2 (right).

(D) Untransplanted *Csf1r*$^{-/-}$ mouse lacks teeth (top), while transplanted *Csf1r*$^{-/-}$ mouse shows tooth growth (bottom).

(E and F) Both *Ccr2* Rfp/Rfp BM (E) and purified BM monocytes (F) engraft in the *Csf1r*$^{-/-}$ brain and express TMEM119 at T = 21 days. Scale bar, 100 μm.

See also Figure S3.

The CNS Environment Strongly and Rapidly Induces Microglial Gene Expression in CNS Naive Cells

The ability of both HSC- and YS-derived donor cells to engraft in the brain parenchyma and express TMEM119 only when engrafted attests to the potency of programming signals from the brain parenchyma. To comprehensively measure the ability of diverse transplanted cells to adopt a microglial transcriptional program, we purified parenchymal TMEM119+ MLCs using identical methods to transplanted microglia, allowing highly specific isolation of parenchymal macrophages. We transcriptionally profiled MLCs derived from E8 yolk sac, E12–E13 fetal brain, E13–E14 fetal liver, adult blood, and BM, comparing them to each other and to transplanted microglia. Among these highly purified transcriptomes, we observed a striking degree of similarity between engrafted cell types (Figures 4A and S4A–S4C). MLCs, irrespective of ontogeny, expressed many microglia signature genes, including *Tmem119*, *Fcrls*, *Hexb*, and *Olfml3*, at near-microglial levels (Figure 4A). Gene expression in all MLC types was well correlated (Spearman coefficients >0.6–0.8), and in exploratory analyses combining published datasets, MLCs were more closely related to microglia than to other tissue macrophages, monocytes, or neutrophils (Figures S4C and S4D). These data confirm the strong programming effects of the brain parenchyma on macrophages, and the intrinsic ability of even CNS-alien macrophages to respond to programming signals by expressing microglial genes.

2010) into *Csf1r*$^{-/-}$ mice leads to robust TMEM119+ MLC engraftment at 2 weeks, meaning that CCR2 is dispensable in this system (Figure 3E). Interestingly, we observed a range of RFP fluorescence levels in engrafted cells (Figure S3D), suggesting that either brain signals suppress CCR2 expression or more than one population of BM cells (as distinguished by CCR2 reporter expression) is capable of brain engraftment. We also noted a preponderance of RFP+ cells in a periventricular distribution (Figure S3E). Finally, to determine whether myeloid progenitors or HSCs were strictly required to create MLCs, we also transplanted BM monocytes that were stringently depleted of progenitor populations (Figure S3F) and observed abundant TMEM119+ parenchymal MLCs by 2 weeks (Figure 3F).

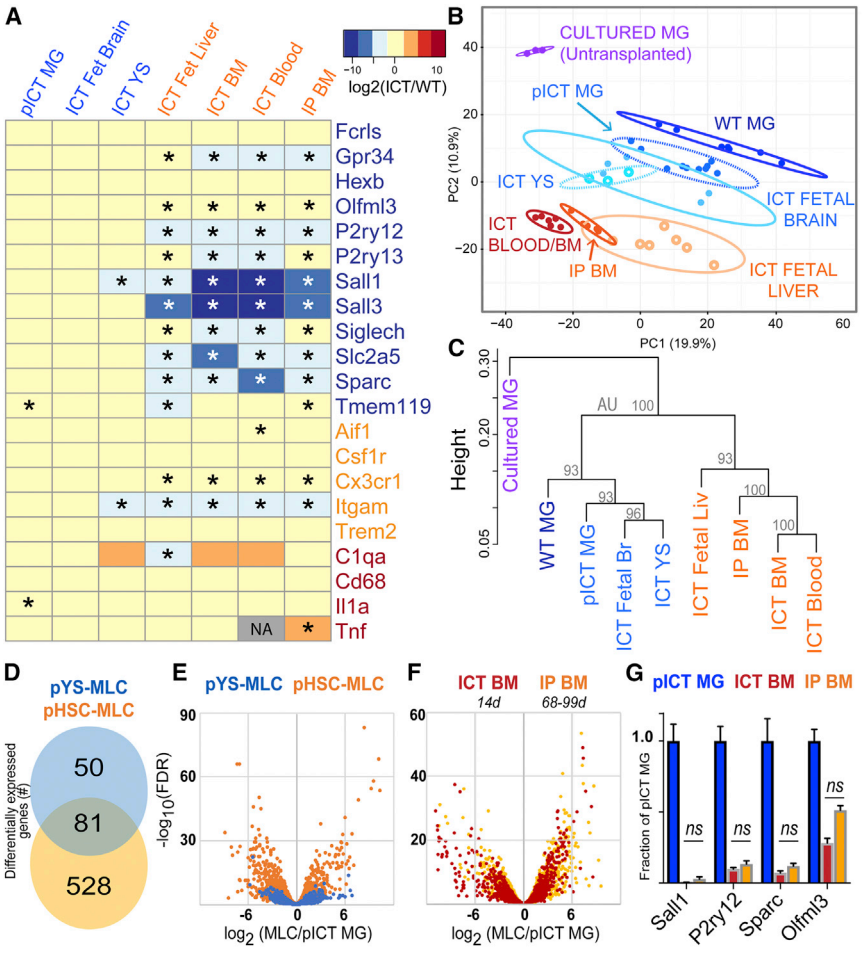

Figure 4. Ontogeny Shapes Adoption of Microglial Transcriptional Identity; BM-Derived Cells Show Highly Similar Transcriptomes at 2 Weeks Compared to 2–3 Months of Brain Residence

(A) Heatmap showing log2(FC versus WT) expression of microglial (blue), myeloid (orange), and reactivity (red) genes across MLC types. *FDR < 0.05 compared to WT. Gray box indicates that edgeR algorithm could not compute log2(FC) due to low read abundance.

(B) Plot of largest principal components for cultured microglia (purple), WT microglia (dark blue), pooled ICT MG (blue), YS-MLCs (ICT yolk sac, fetal brain; lighter shades of blue), fetal liver MLCs (light orange), and HSC-MLCs (ICT blood, BM, and BMT; orange/red), using top 2,500 most variant genes. Ellipses demarcate 95% confidence interval for assigned clusters.

(C) Unsupervised hierarchical clustering of microglia, pooled ICT microglia, and MLCs by Spearman coefficients using 1,000 most variant genes. AU, approximately unbiased p value using PVclust package; bootstrap, n = 10,000.

(D) Venn diagram showing differential gene expression between pooled YS- and HSC-MLCs, both compared to pooled ICT-MGs (2-fold cutoff, FPKM > 20, FDR < 0.05). See also Figure S5A.

(E) Volcano plot overlay showing differential gene expression of YS- and HSC-MLCs types compared to ICT-MGs, measured as log2(pMLC/pMG).

(F) Volcano plot overlay comparing MLCs derived from ICT BM at 14 days (red) to MLCs from i.p. BM at 2–3 months (orange) showing no gross shift in transcriptome difference from microglia.

(G) Microglial identity genes do not change between ICT BM (red) and i.p. BM (orange); ns, FDR > 0.05 by edgeR comparison. Error bars represent SEM. See also Figure S5C. MG, microglia; MLC, microglia-like cell; ICT, intracerebral transplant; HSC, hematopoietic stem cell; YS, yolk sac; pYS, pooled YS; Fetal Br, fetal brain; Fetal Liv, fetal liver; IP BM, intraperitoneal BM transplant.
See also Figures S4 and S5.

HSC Ontogeny Prevents Full Adoption of Microglial Identity

Although grossly similar, we found major ontogeny-dependent differences between HSC- and YS-MLCs. Principal component analysis showed that the transcriptomes of transplanted microglia, YS-MLCs, and fetal brain MLCs overlap with each other, distinct from blood, BM, and fetal liver MLCs (Figure 4B). Unsupervised hierarchical clustering similarly showed that YS-derived (YS, fetal brain) MLC gene expression is more closely related to transplanted microglia than HSC-derived (blood, BM) and mixed-origin MLCs (fetal liver) (Figure 4C).

To focus on ontogeny-specific gene expression patterns, we pooled gene expression data from YS- and HSC-MLC donor groups, excluding fetal liver MLCs since E13–E14 liver contains a mix of YS- and HSC-derived cells (Hoeffel et al., 2015; Gomez Perdiguero et al., 2015). As a group, YS-lineage MLCs had 131 differentially regulated genes compared to transplanted microglia, while HSC-MLCs had 609 (Figure 4D). Volcano plot overlay further depicts the higher similarity of YS-MLCs to transplanted microglia at a whole-transcriptome level (Figure 4E). At the gene level, YS-MLCs expressed microglia signature genes more faithfully than their HSC-derived counterparts, including *Slc2a5*, *Olfml3*, *Gpr34*, *Sparc*, and *P2ry12* (Figure S5A). Among microglia-enriched genes in TMEM119+ cells from a prior study (Bennett et al., 2016), YS-MLCs were significantly closer to microglial expression levels in 30 of 32 measured genes (Table S2). Similarly, among 31 genes enriched in non-microglia CNS myeloid cells, YS-MLCs were closer to microglial levels for 29 (Table S3). Of particular significance, HSC-MLCs did not express *Sall1*, a transcription factor recently implicated in microglial identity (Buttgereit et al., 2016). Interestingly, the pattern of *Sall1* expression by YS-MLCs correlated with its expression during microglial development, from low levels in YS-MLCs, intermediate levels in fetal brain MLCs, and highest in transplanted microglia (Figure S5B).

While YS-MLCs were able to express all microglial signature genes by 2 weeks, HSC-MLCs were not. Based on prior studies using microglial repopulation systems (Bruttger et al., 2015; Mildner et al., 2007; Priller et al., 2001; Varvel et al., 2012), along

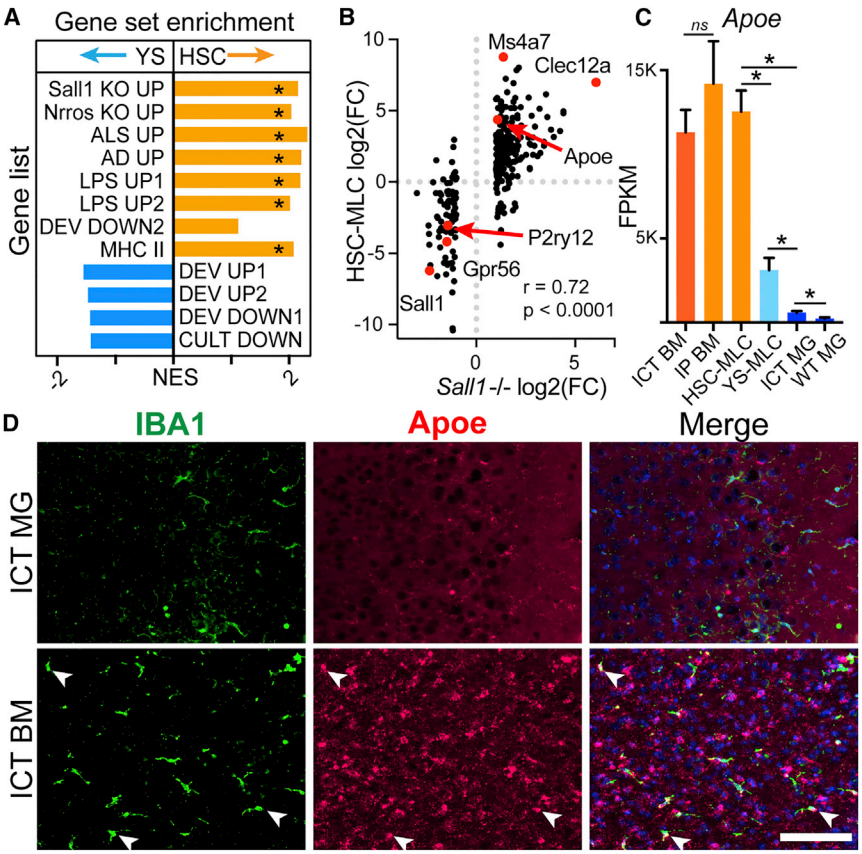

Figure 5. HSC-MLCs Resemble Microglia Lacking Identity Genes and in Disease States

(A) Normalized enrichment scores (NESs) from gene set enrichment analysis (GSEA) comparing YS- to HSC-MLCs for enrichment in genes upregulated in *Sall1*$^{-/-}$ (Sall1 KO UP), *Nrros*$^{-/-}$ (Nrros KO UP), ALS (ALS UP), AD (AD UP), after LPS treatment (LPS UP1, 2), changed in during development (DEV UP 1, 2 or DEV DOWN1, 2), in culture (CULT DOWN), and MHCII genes. *FDR < 0.05.

(B) Expression plot comparing HSC-MLCs and *Sall1*$^{-/-}$ microglia, both expressed as log2(FC/WT). Red dots highlight genes of interest. r, correlation coefficient; p, p value for linear regression analysis.

(C) *Apoe* gene expression in MGs/MLCs. *FDR < 0.05. Error bars represent SEM.

(D) RNA *in situ* hybridization for *Apoe* (red) with IBA1 counterstain in *Csf1r*$^{-/-}$ brains 14 days post-transplantation with BM or microglia. Arrows indicate *Apoe*+ MLCs. Scale bar, 100 μm.

See also Figure S5.

with observations in other tissues (Scott et al., 2016; van de Laar et al., 2016), we felt it was critical to address whether longer CNS engraftment was sufficient to better reprogram HSC-MLCs into microglia. If so, one would expect interval increases in the expression of microglial signature genes with prolonged brain engraftment, akin to observations in the liver between 15 and 30 days after engraftment (Scott et al., 2016). We therefore analyzed MLCs that were engrafted in the brain parenchyma of rescued mice for 2–3 months (mean 81 days) following peripheral BM transplantation, and assessed for a trajectory of higher expression of microglial identity genes. We compared gene expression patterns to directly injected BM-MLCs harvested after 14 days and found almost no interval induction of microglia signature genes after prolonged CNS incubation. In particular, longer-term engrafted cells showed persistently low expression of *Sall1*, *Sall3*, *Sparc*, *P2ry12*, *Gpr34*, and *Olfml3*, none of which were statistically different from expression in short-term engrafted cells (Figures 4A, 4G, and S5C). By unbiased clustering, long-term engrafted BM-MLCs were highly similar to short-term engrafted BM and blood MLCs (Figures 4B and 4C). Volcano plot overlay does not show increased similarity of longer-term engrafted cells to microglia (Figure 4F). Longer-term engraftment was associated with differential gene expression (Tables S4 and S5), though with no clear evidence of further reprogramming based on microglia signature genes (Figure S5C). Taken together, these data show that when macrophages derived from HSCs engraft in the brain, they become similar to microglia by 14 days, but do not further increase expression of microglial identity genes when incubated in the brain at least four times longer. In contrast, YS-derived macrophages, which share a common ancestor with microglia, have the intrinsic potential to become highly similar to transplanted microglia by 14 days.

HSC-MLCs Share Transcriptional Signatures with Disease-Associated Microglia, Including Highly Elevated *Apoe* Expression

To better understand transcriptomic differences between HSC- and YS-MLCs, we assessed transcriptional networks by multiple approaches. Pathway analysis (Ingenuity) suggested HSC-MLCs were enriched in pathways associated with CNS perturbation (neuroinflammatory signaling, NOS/ROS production, and TLR signaling; Figure S5D). Recent studies of mouse and human microglia found significant overlap between transcriptional changes in cultured, Alzheimer's disease (AD), amyotrophic lateral sclerosis (ALS), LPS exposed, and immature microglia, suggesting common downstream reactivity pathways (Bohlen et al., 2017; Gosselin et al., 2017). We wondered if the observed gene expression differences between HSC- and YS-MLCs overlapped with differences between brain myeloid cells in disease compared to health. Indeed, HSC- compared to YS-MLCs were significantly enriched in gene sets associated with ALS, AD, LPS treatment, immaturity, and *in vitro* culture from prior studies (Bennett et al., 2016; Chiu et al., 2013; Matcovitch-Natan et al., 2016; Wang et al., 2015), along with major histocompatibility complex class II genes (Figure 5A). YS-MLCs were relatively enriched in gene sets associated with homeostasis, but

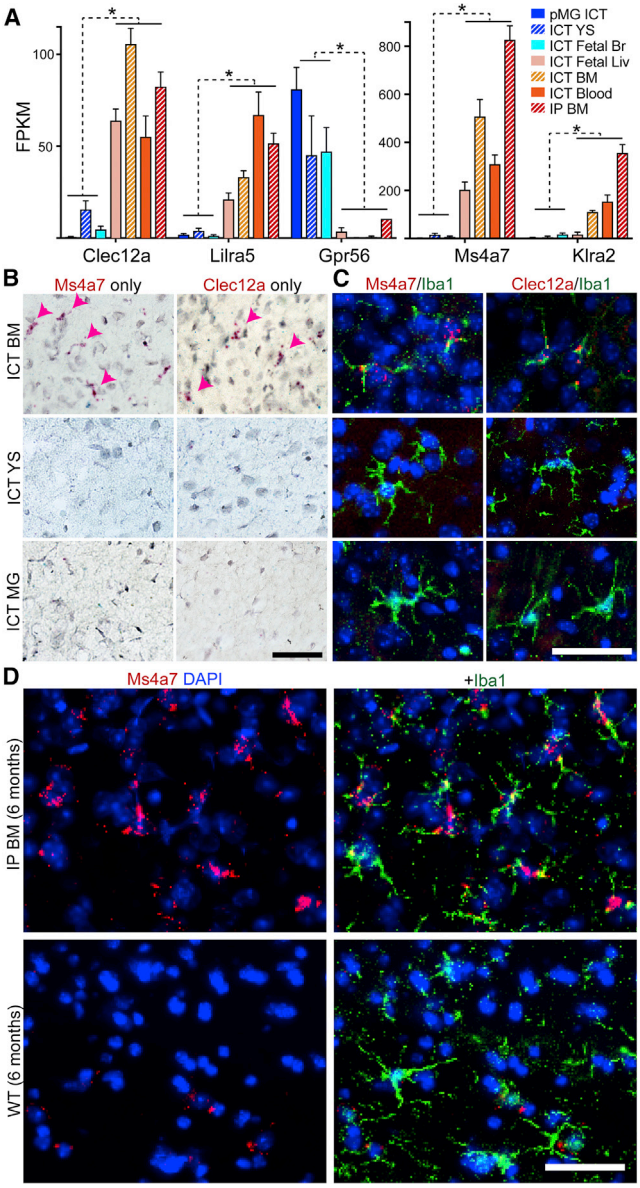

Figure 6. Ontogeny Markers Discriminate HSC- from YS-MLCs and Microglia

(A) FPKM values for HSC- and YS-MLC/MG enriched genes (red-orange and blue bars, respectively). Error bars represent SEM, *FDR < 0.005 for all genes between YS/MG and HSC groups.

(B) RNA *in situ* hybridization showing expression of *Ms4a7* or *Clec12a* (red) in ICT BM-MLCs, but not YS-MLCs or ICT MGs. Arrowheads highlight BM-MLCs. Scale bar, 50 μm.

(C) Fluorescent RNA *in situ* hybridization showing expression of *Ms4a7* or *Clec12a* (red) in ICT BM-MLCs, but not YS-MLCs or ICT MGs, co-stained for IBA1 (green). Scale bar, 50 μm.

(D) RNA *in situ*s show persistent expression of *Ms4a7* (red) in IBA1+ cells (green) 6 months after transplantation in HSC-MLCs, but no expression in WT microglia. Scale bar, 50 μm.

See also Figures S5 and S6.

these did not reach significance cutoff (false discovery rate [FDR] < 0.05).

Since HSC-MLCs lack *Sall1*, we also tested for enrichment of genes that change with loss of microglial *Sall1* and *Nrros*, which were recently found to cause similar shifts in transcriptional identity (Buttgereit et al., 2016; Wong et al., 2017). We compared our datasets to published gene expression profiles of *Sall1*- and *Nrros*-deficient microglia, and indeed HSC-MLCs showed significant enrichment for genes upregulated in both *Sall1* and *Nrros*$^{-/-}$ microglia (Figure 5A). In fact, gene expression in HSC-MLCs and *Sall1*$^{-/-}$ microglia was highly correlated (Figure 5B), suggesting that lack of *Sall1* could contribute to differential gene expression in HSC-MLCs.

Among these dysregulated genes, *Apoe* stands out as the most highly expressed gene in HSC-MLCs, and does not decrease with longer engraftment (Figure 5C). To validate high *Apoe* expression observed in HSC-MLCs, we performed RNA *in situ* hybridization. As anticipated, we found high-intensity signal in many brain macrophages after BM, but not microglia, ICT. Surprisingly, we also found increased probe signal throughout the brain parenchyma in IBA1-negative cells of BM ICT animals, which may reflect increased expression by astrocytes in the presence of HSC-MLCs (Figure 5D). Taken together, these results show that HSC-MLCs, but not YS-MLCs or transplanted microglia, share gene expression signatures with microglia in disease states or after loss of identity genes.

HSC-MLCs Express Markers Distinct from YS-MLCs and Microglia

The *Csf1r*$^{-/-}$ transplantation approach demonstrates that many macrophage types have the intrinsic potential to masquerade as microglia by expressing signature genes and TMEM119 protein in the brain. This does not occur following conventional BMT (Bennett et al., 2016) and complicates the use of microglia signature genes to distinguish microglia from HSC-MLCs in complex disease models, requiring creation of new tools. To identify stable markers of brain parenchymal macrophage ontogeny, we screened our dataset for genes (1) highly expressed across HSC-MLC types, but lowly expressed in YS-MLCs and microglia, or (2) highly expressed in YS-MLCs and microglia, but not HSC-MLCs. We then eliminated genes dysregulated in microglia in AD and after LPS stimulation, yielding five candidate ontogeny markers: *Clec12a*, *Ms4a7*, *Lilra5*, *Klra2*, and *Gpr56* (Figure 6A). We performed RNA *in situ* hybridization to validate the localization of *Ms4a7*, *Clec12a*, and *Gpr56* in engrafted brain tissues (Figures 6B–6D and S6A). As predicted by transcriptomic data, virtually all HSC-MLCs, but no microglia or YS-MLCs, were *Ms4a7*+ and *Clec12a*+. Meanwhile, no HSC lineage cells were *Gpr56*+, a gene recently associated with microglial ontogeny in transcriptomic studies (Gosselin et al., 2014) and also expressed by other glia, such as astrocytes (Zhang et al., 2014). Importantly, we probed healthy postnatal CNS tissue and did not find *Ms4a7* expression by microglia across the lifespan (Figure S6C). We also tested whether these HSC ontogeny markers were unique to the *Csf1r*$^{-/-}$ system. We transplanted GFP+ BM directly into the CNS of neonatal and adult *Cx3cr1-CreER*$^{+/-}$; *Csf1r*$^{fl/fl}$ mice, treated with tamoxifen, to partially and transiently deplete

microglia. At 2 months, we observed abundant GFP+ TMEM119+ cells in the brain parenchyma and concordant clusters of *Ms4a7*+ cells by RNA *in situ* (Figures S6D–S6G), suggesting that HSC ontogeny marker induction is unique to neither the *Csf1r*$^{-/-}$ mouse system nor the neonatal CNS.

Since ICT transplanted *Csf1r*$^{-/-}$ animals do not survive long enough to test prolonged time points, we also tested whether HSC-MLCs in animals rescued by i.p. BMT were able to downregulate *Ms4a7* 6 months after transplantation, as would be expected if environmental signals superseded the limits of ontogeny. We found that all HSC-MLCs remained TMEM119+ and *Ms4a7*+ after 6 month incubation (Figures 6D and S6B). This is consistent with our transcriptomic observations at 2–3 months, when HSC-MLCs sustained expression of ontogeny markers, and in fact increased expression of one such ontogeny marker, *Klra2* (Figure S5C). In sum, we capitalized on transcriptomic data from transplanted brain macrophages to validate ontogeny markers that are stable despite the high plasticity of brain macrophage gene expression in response to the CNS environment.

MS4A7 Is Specific to Human HSC-MLCs and Found in Human Alzheimer's Disease

To explore the utility of this transplantation system for human brain macrophage study, we crossed *Csf1r*$^{+/-}$ mice into an immunodeficient strain expressing the human form of MCSF (Rathinam et al., 2011), based on our observations that murine MCSF does not promote human microglial survival (unpublished data), creating a *Rag2*$^{-/-}$ *IL2rg*$^{-/-}$ *hMCSF Csf1r*$^{-/-}$ mouse. We transplanted human blood, fetal brain macrophages, and postnatal microglia from neurosurgical cases directly into the mouse CNS. We observed engraftment, survival, and ramification of all cell types, often over large territories of the mouse brain parenchyma (Figures 7A–7D). Nearly all transplanted human fetal and postnatal brain parenchymal macrophages were TMEM119 immunoreactive (Figures 7C and 7D), whereas engrafted peripheral blood cells showed variable staining: in some animals, nearly all engrafted blood-derived cells were TMEM119+ (Figure 7A), while in others, expression was restricted to a fraction (Figure 7B).

To better study human microglia, we generated a mouse monoclonal antibody against the extracellular domain of human TMEM119 using the same approach we recently used for mouse TMEM119 (Bennett et al., 2016). This custom antibody does not stain human blood (Figure S7A), but does identify a distinct subpopulation of CD45+/CD11B+ cells in human brain cell suspensions (Figure S7B), as well as human fetal brain macrophages engrafted in the mouse brain (Figures 7E and S7C). This tool will allow specific purification of human microglia in the future.

Finally, we wondered whether *MS4A7* has potential for use as an ontogeny marker for human brain macrophages. We found that transplanted blood-derived human HSC-MLCs, but not microglia, were MS4A7 immunoreactive (Figures 7F–7H and S7D–S7F). Having demonstrated that MS4A7 can identify human HSC-MLCs, we next tested if we could detect putative HSC-MLCs in a complex human disease. In postmortem samples from cases of AD and severe cerebrovascular disease, we observed rare ramified *TMEM119*+/*MS4A7*+/IBA1+ cells, which we could not detect in healthy controls (Figures 7I, 7J, S7G, and S7H). Interestingly, we also found frequent *MS4A7*+/IBA1+ cells in a perivascular distribution that were not associated with disease (Figures 7K and S7I). Together, these findings demonstrate that MS4A7 is a conserved ontogeny marker, and that the presence of HSC-MLCs may be associated with human neurodegenerative disease.

DISCUSSION

Direct CNS Transplantation Reveals Fundamental Principles of Microglial Identity and Plasticity

Ex vivo manipulations cause dramatic shifts in microglial gene expression that resemble patterns found during disease and in immature embryonic microglia (Bohlen et al., 2017; Gosselin et al., 2014, 2017; Haynes et al., 2006). Using a cell transplantation system, we found that upon return to the CNS, microglia readily inhabit the *Csf1r*$^{-/-}$ brain, adopt a ramified morphology, and revert to a normal transcriptional program despite profound *ex vivo* derangement. Our findings demonstrate that though remarkably sensitive to environment, microglia robustly retain the potential to return to a homeostatic state. Comparison between transplanted mature, young, and cultured microglia clarifies that the brain is replete with necessary factors to sustain, induce, and re-induce homeostatic microglial gene expression. These findings have direct relevance to microglial reactivity and development of myeloid cell therapies for brain disease. They suggest that microglia themselves could be cultured, modified, and used translationally for CNS cell therapies, and further, identify the parenchymal macrophage niche as a valid "*in vivo* culture system" for transplanted microglia. Our findings also encourage continued efforts to develop an *in vitro* culture system that better sustains microglial identity.

The CNS Induces Microglial Gene Expression in Diverse Myeloid Populations

Cell depletion and BMT studies demonstrate the brain's ability to host peripheral myeloid cells (Bruttger et al., 2015; Cronk et al., 2018; Mildner et al., 2007; Priller et al., 2001). Here, we show that the *Csf1r*$^{-/-}$ brain readily and durably hosts myeloid cells from blood, BM, fetal liver, fetal brain, and yolk sac. We found strong induction of microglial signature genes and TMEM119 protein within 14 days, by as yet unknown CNS environmental cues. Combining observations using BMT and/or genetic microglial ablation with our study, macrophages likely also need access to an open parenchymal macrophage niche (Bruttger et al., 2015; Cronk et al., 2018). Here, without conditioning irradiation or chemotherapy, we were able to directly compare multiple engrafted TMEM119+ populations from the YS and HSC lineages at multiple stages of development, to clearly delineate the consequences of ontogeny on gene expression in brain resident macrophages.

Peripheral BM Injection Rescues *Csf1r*$^{-/-}$ Animals and Results in Pervasive Engraftment of Brain Macrophages without Irradiation or Chemotherapy

Intraperitoneal injection of whole BM with no preconditioning prolongs the survival of *Csf1r*$^{-/-}$ mice, which typically succumb

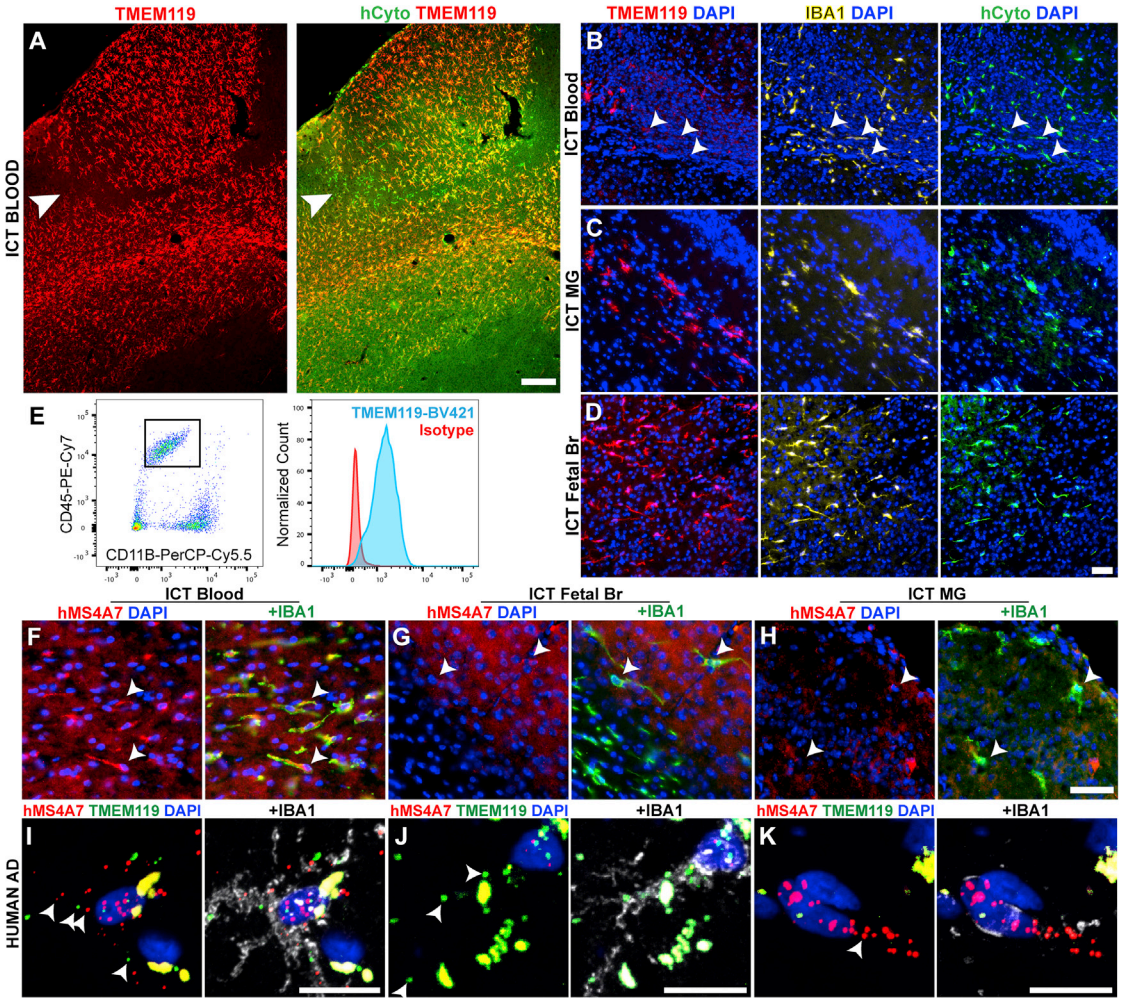

Figure 7. Macrophage Transplantation, Origin Markers, and Anti-TMEM119 Monoclonal Antibodies for the Study of Primary Human Macrophages *In Vivo*

(A) Pervasively engrafted TMEM119+ (red) cells from human blood in the *Rag2*$^{-/-}$*Il2rg*$^{-/-}$*hMCSF*$^{+/+}$*Csf1r*$^{-/-}$ brain parenchyma, co-stained with human cytoplasm marker (hCyto, green). Arrowhead indicates TMEM119− cells at edge of engraftment territory. Scale bar, 200 μm.

(B–D) Representative images of MLCs from human blood (B), adult microglia (C), and cultured fetal brain (D), immunostained for human TMEM119 (red), IBA1 (yellow), and human cytoplasmic marker (green). Arrowheads in (B) identify human TMEM119 low/− cells. Scale bar, 50 μm.

(E) A custom anti-human TMEM119 antibody identifies hCD45+/CD11B+ fetal human MLCs 14 days after transplantation into the mouse CNS. Tmem119 staining (blue) is shown compared to isotype control (red).

(F–H) Representative images of MLCs from blood (F), fetal brain (G), and primary human microglia (H) immunostained for human MS4A7 (red) and IBA1 (green). Arrowheads (B and F–H) mark location of IBA1+ cell bodies. Scale bar, 100 μm.

(I–K) Representative images from RNA *in situ* hybridization of postmortem AD brain samples, showing (I) rare *MS4A7*+(red)/*TMEM119*+(green)/IBA1 protein+ (white) macrophages, (J) abundant *MS4A7*−/*TMEM119*+/IBA1+ macrophages, and (K) MS4A7+/TMEM119−/IBA1+ perivascular macrophages. Arrowheads show examples of positive puncta, given abundant autofluorescent signal (puncta in perfect registration). Scale bars, 12.5 μm.

See also Figure S7.

around 2 weeks of life (Dai et al., 2002; Li et al., 2006). In rescued animals, we observed pervasive engraftment of donor cells in all tissues examined, including the brain and spinal cord. Surprisingly, although classic studies identify CCR2 as critical for CNS entry in the setting of inflammation, (Ajami et al., 2011; 2007), we find that MLC engraftment did not depend on CCR2, nor did the *Csf1r*$^{-/-}$ host show evidence for frank BBB breakdown. These data suggest the existence of an alternative mechanism for cell entry into the brain. Furthermore, we found that isolated BM monocytes themselves can become TMEM119+ MLCs, consistent with recent results using conditional *Csf1r* deletion to deplete microglia (Cronk et al., 2018). Though this does not exclude the possibility that myeloid progenitors or HSCs also contribute to MLC formation, it suggests monocytes as a candidate donor population for cell-based therapies. Provocatively, circulating cells do not contribute to repopulation following pharmacologic depletion of microglia (Huang et al., 2018), suggesting that surviving host microglia, which are absent in *Csf1r*$^{-/-}$ hosts,

may be advantaged colonizers and/or limit parenchymal macrophage niche access.

Ontogeny Regulates Adoption of Microglial Identity and Is Revealed by Stable Markers

Direct CNS injection allowed detailed and controlled exploration of fundamental differences between microglia and MLCs from multiple ontogenies across development. Although all MLC types shared similarities with microglia, we observed major effects of ontogeny on transcriptomic identity. YS-MLCs, which share a common progenitor with microglia, became more microglia-like than HSC-MLCs, notably in their expression of microglial signature genes. These findings contrast observations in lung, where engrafted yolk sac, fetal liver, and BM monocytes were reported to be nearly identical to alveolar macrophages (van de Laar et al., 2016).

Since *Tmem119* and other microglial markers may be expressed by HSC-MLCs, their presence does not assure microglial ontogeny. Here, we validated a panel of HSC ontogeny markers that are homogenously expressed among engrafted cells. Despite exposure to the same CNS signals, HSC-MLCs, but not YS-MLCs/microglia, express *Ms4a7*, *Clec12a*, *Klra2*, and *Lilra5*. In contrast, HSC-MLCs do not express *Gpr56*, which is expressed by most, if not all, YS-MLCs/microglia. These ontogeny markers may augment current origin-mapping approaches such as parabiosis and genetic fate labeling. Interestingly, while *Clec12a*, *Lilra5*, and *Klra2* are broadly expressed by circulating and tissue myeloid cells, *Ms4a7* expression is restricted to macrophages (Heng et al., 2008). It is highly expressed by intestinal macrophages, which increasingly arise from HSCs in adulthood (Bain et al., 2014), raising the possibility that ontogeny markers may be valid outside of the CNS.

YS-MLCs were able to express the full complement of known microglial identity genes by 14 days, but HSC-MLCs were not. An important caveat to the *Csf1r*$^{-/-}$ system is the limited ability to study MLCs at long time points after transplantation due to host viability. Peripheral BM injection permitted comparison of long- to short-term resident HSC-MLCs to determine whether prolonged CNS residence further promoted microglial gene expression. We found surprisingly little difference between HSC-MLCs at 14 days versus 2–3 months using both unbiased and targeted analyses. In particular, HSC-MLCs remained unable to express *Sall1*/*Sall3*; did not further increase expression of signature genes such as *Tmem119*, *P2ry12*, and *Olfml3*; and continued to express HSC ontogeny markers, some at increased levels. After 6 months of brain residence, HSC-MLCs continued to express *Ms4a7*, which also marked HSC-MLCs in both neonatal and adult tamoxifen-treated *Cx3cr1-CreER;Csf1r*$^{fl/fl}$ hosts after 2 months. Taken together, these observations suggest that prolonged CNS incubation is not sufficient to completely override cell-intrinsic properties associated with ontogeny, an important consideration for the development of myeloid cell therapies for brain disease. The limitations of the *Csf1r*$^{-/-}$ model, or in fact any mouse model, call for future studies to determine if years-long incubation relevant for human lifespan is sufficient to fully induce microglial identity in HSC-derived cells.

HSC-MLCs Resemble Microglia in Disease States

Sall1 and *Nrros* are central to microglial identity, and when absent, microglia adopt an abnormal phenotype characterized by reduced expression of microglial signature genes and increased expression of macrophage markers associated with inflammation (Buttgereit et al., 2016; Wong et al., 2017). HSC-MLCs are unable to express *Sall1* in *Csf1r*$^{-/-}$ hosts and resemble microglia from multiple disease states. Of particular interest, *Apoe* is the most highly expressed gene in HSC-MLCs—4–20 times higher than in transplanted microglia or YS-MLCs. By *in situ* hybridization, HSC-MLC engrafted brains also showed increased *Apoe* levels in other brain cell types in addition to microglia. *Apoe* genotype remains one of the most important risk factors in AD, and may directly drive microglial dyshomeostasis during neurodegeneration (Krasemann et al., 2017; Shi et al., 2017).

Intriguingly, HSC-MLC ontogeny markers from our study have previously been implicated in neurodegenerative processes. The *MS4A* family of genes is associated with AD risk in large human studies (Hollingworth et al., 2011). In addition, *Clec12a* blockade attenuated a mouse model of multiple sclerosis (Sagar et al., 2017). Associations between HSC transcriptomes, ontogeny markers, and brain disease raise the tantalizing hypothesis that infiltrating cells could masquerade as microglia and contribute to brain malfunction. The future study of the functional consequences of HSC-MLCs and different ontogeny markers may be critical to understanding brain function in health and disease.

Transplantation of Primary Human Cells and a Custom Anti-human Tmem119 Antibody Facilitate Study of Human Microglia and MLCs

In vitro studies of human microglia are limited by loss of microglial identity in culture. Here, we found that cultured and acutely isolated primary cells from human blood and brain engraft, ramify, and express TMEM119 in humanized *Csf1r*$^{-/-}$ rodent brains. This shows that the murine brain is replete with factors to support survival of primary human macrophages and expression of a microglial protein not reliably detectable in culture (Abud et al., 2017; Gosselin et al., 2017). It also offers a new approach to studying human microglia in a living and highly controllable CNS environment that we hope will facilitate future studies of disease. Since blood from patients with brain diseases is relatively accessible, direct CNS transplantation may be used to compare MLCs from healthy and disease states, complementing analogous approaches limited by lack of microglial gene expression *in vitro* (Gosselin et al., 2017; Ohgidani et al., 2014; Sellgren et al., 2017). We also validated a custom anti-human TMEM119 antibody for FACS of pure human microglia from human and xenograft samples, for use by the microglia community.

Of equal importance, we confirmed that MS4A7 marks human HSC-MLCs, but not microglia, suggesting that it is an ontogeny marker across species. The relevance of infiltrating myeloid cells to human brain disease is unresolved but of great consequence to the development of novel therapies. Since parabiosis and fate-labeling are not possible in human, *MS4A7* may offer a feasible approach to detecting long-term resident HSC-MLCs in

the CNS. Importantly, we found *MS4A7+/TMEM119+* cells in brains of neurodegenerative disease patients, but not healthy controls, demonstrating the feasibility of this method and supporting the possibility that infiltrating myeloid cells may reside in the degenerating human brain.

Relevance of Ontogeny and Environment to Microglia Replacement Therapy

Here, we provided new tools to study transplanted mouse and human brain macrophages, and applied them to relationships between environment, ontogeny, and tissue macrophage identity. In addition to the future studies discussed above, direct myeloid cell transplantation holds potential as a form of treatment for diverse neurological and psychiatric diseases. Our results reveal the importance of both ontogeny and CNS environmental cues to brain resident macrophage identity, as well as potential future avenues for understanding the CNS macrophage niche. These findings warrant future studies to reveal the functional and phenotypic consequences of these important differences, in order to make robust human microglial replacement therapies a reality.

STAR★METHODS

Detailed methods are provided in the online version of this paper and include the following:

- KEY RESOURCES TABLE
- CONTACT FOR REAGENT AND RESOURCE SHARING
- EXPERIMENTAL MODEL AND SUBJECT DETAILS
  - Mouse Models
  - Human tissue samples
- METHOD DETAILS
  - General considerations for experimental design
  - Microglia/MLC transplantation
  - Donor tissue preparation
  - Flow cytometry
  - RNaseq library construction and sequencing
  - Anti-human Tmem119 antibody generation
  - Tissue Immunostaining
  - RNA *in situ* hybridization
  - Image acquisition and processing
  - Analysis of RNaseq data
  - Replicates
- QUANTIFICATION AND STATISTICAL ANALYSIS
- DATA AND SOFTWARE AVAILABILITY

SUPPLEMENTAL INFORMATION

Supplemental Information includes seven figures and seven tables and can be found with this article online at https://doi.org/10.1016/j.neuron.2018.05.014.

ACKNOWLEDGMENTS

We thank the B.A.B. laboratory, particularly C. Bohlen, S. Sloan, L. Clarke, S. Liddelow, L. Sun, and T. Li, for feedback and consultation; G. Smerin and K. Guttenplan for tissue samples; L.B. Torres for *Ccr2* Rfp and R. Stanley for *Csf1r*$^{-/-}$ animals; N. Allen, T. Wyss-Coray, and H. Nakauchi for feedback and mentoring; the Stanford Shared FACS Facility, supported by NIH S10RR025518-01; A. Olson and the Stanford Neuroscience Microscopy Service, supported by NIH NS069375; the Stanford Alzheimer Disease Research Center for providing human samples, supported by NIH P50AG047366; and P. Taylor, C. Wang, and K. Cohane for TMEM119 antibody collaboration. This work was funded by NIH R37DA01504317 (to B.A.B.); NRSA predoctoral fellowship F31 NS078813 (to M.L.B.); training grants T32MH019938-22 and K08MH112120 (to F.C.B.), K08NS901527 and R01CA216054-01 (to M.H.G.), and K08 NS075144 (to G.A.G.); the JPB Foundation grant 853 (to B.A.B.); the Dr. Miriam and Sheldon G. Adelson Medical Research Foundation grant 04-7023433 (to B.A.B.); and Vincent and Stella Coates. To B.A.B., who forever changed our lives, science, and society: thank you, and we miss you.

AUTHOR CONTRIBUTIONS

Conceptualization, F.C.B., B.A.B., and M.L.B.; Methodology, F.C.B. and M.L.B.; Formal Analysis, F.C.B. and M.L.B.; Investigation, F.C.B., M.L.B., S.B.M., and F.Y.; Resources, G.A.G., M.H.G., and E.D.P.; Data Curation, F.C.B.; Writing – Original Draft, F.C.B.; Writing – Review & Editing, F.C.B. and M.L.B.; Visualization, F.C.B. and M.L.B.; Supervision, B.A.B. and F.C.B.; Project Administration, F.C.B.; Funding Acquisition, B.A.B., F.C.B., and M.L.B.

DECLARATION OF INTERESTS

The authors declare no competing interests.

Received: December 1, 2017
Revised: January 2, 2018
Accepted: May 7, 2018
Published: May 31, 2018

REFERENCES

Abud, E.M., Ramirez, R.N., Martinez, E.S., Healy, L.M., Nguyen, C.H.H., Newman, S.A., Yeromin, A.V., Scarfone, V.M., Marsh, S.E., Fimbres, C., et al. (2017). iPSC-derived human microglia-like cells to study neurological diseases. Neuron *94*, 278–293.e9.

Ajami, B., Bennett, J.L., Krieger, C., Tetzlaff, W., and Rossi, F.M.V. (2007). Local self-renewal can sustain CNS microglia maintenance and function throughout adult life. Nat. Neurosci. *10*, 1538–1543.

Ajami, B., Bennett, J.L., Krieger, C., McNagny, K.M., and Rossi, F.M.V. (2011). Infiltrating monocytes trigger EAE progression, but do not contribute to the resident microglia pool. Nat. Neurosci. *14*, 1142–1149.

Bain, C.C., Bravo-Blas, A., Scott, C.L., Perdiguero, E.G., Geissmann, F., Henri, S., Malissen, B., Osborne, L.C., Artis, D., and Mowat, A.M. (2014). Constant replenishment from circulating monocytes maintains the macrophage pool in the intestine of adult mice. Nat. Immunol. *15*, 929–937.

Bardou, P., Mariette, J., Escudié, F., Djemiel, C., and Klopp, C. (2014). jvenn: an interactive Venn diagram viewer. BMC Bioinformatics *15*, 293.

Bennett, M.L., Bennett, F.C., Liddelow, S.A., Ajami, B., Zamanian, J.L., Fernhoff, N.B., Mulinyawe, S.B., Bohlen, C.J., Adil, A., Tucker, A., et al. (2016). New tools for studying microglia in the mouse and human CNS. Proc. Natl. Acad. Sci. USA *113*, E1738–E1746.

Biffi, A., Montini, E., Lorioli, L., Cesani, M., Fumagalli, F., Plati, T., Baldoli, C., Martino, S., Calabria, A., Canale, S., et al. (2013). Lentiviral hematopoietic stem cell gene therapy benefits metachromatic leukodystrophy. Science *341*, 1233158.

Bohlen, C.J., Bennett, F.C., Tucker, A.F., Collins, H.Y., Mulinyawe, S.B., and Barres, B.A. (2017). Diverse requirements for microglial survival, specification, and function revealed by defined-medium cultures. Neuron *94*, 759–773.e8.

Bruttger, J., Karram, K., Wörtge, S., Regen, T., Marini, F., Hoppmann, N., Klein, M., Blank, T., Yona, S., Wolf, Y., et al. (2015). Genetic cell ablation reveals clusters of local self-renewing microglia in the mammalian central nervous system. Immunity *43*, 92–106.

Buttgereit, A., Lelios, I., Yu, X., Vrohlings, M., Krakoski, N.R., Gautier, E.L., Nishinakamura, R., Becher, B., and Greter, M. (2016). Sall1 is a transcriptional

regulator defining microglia identity and function. Nat. Immunol. *17*, 1397–1406.

Chiu, I.M., Morimoto, E.T.A., Goodarzi, H., Liao, J.T., O'Keeffe, S., Phatnani, H.P., Muratet, M., Carroll, M.C., Levy, S., Tavazoie, S., et al. (2013). A neurodegeneration-specific gene-expression signature of acutely isolated microglia from an amyotrophic lateral sclerosis mouse model. Cell Rep. *4*, 385–401.

Clarke, L.E., Liddelow, S.A., Chakraborty, C., Münch, A.E., Heiman, M., and Barres, B.A. (2018). Normal aging induces A1-like astrocyte reactivity. Proc. Natl. Acad. Sci. USA *115*, E1896–E1905.

Cronk, J.C., Filiano, A.J., Louveau, A., Marin, I., Marsh, R., Ji, E., Goldman, D.H., Smirnov, I., Geraci, N., Acton, S., et al. (2018). Peripherally derived macrophages can engraft the brain independent of irradiation and maintain an identity distinct from microglia. J. Exp. Med. *47*, 1–10.

de Chaumont, F., Dallongeville, S., Chenouard, N., Hervé, N., Pop, S., Provoost, T., Meas-Yedid, V., Pankajakshan, P., Lecomte, T., Le Montagner, Y., et al. (2012). Icy: an open bioimage informatics platform for extended reproducible research. Nat. Methods *9*, 690–696.

Dai, X.-M., Ryan, G.R., Hapel, A.J., Dominguez, M.G., Russell, R.G., Kapp, S., Sylvestre, V., and Stanley, E.R. (2002). Targeted disruption of the mouse colony-stimulating factor 1 receptor gene results in osteopetrosis, mononuclear phagocyte deficiency, increased primitive progenitor cell frequencies, and reproductive defects. Blood *99*, 111–120.

Dzenko, K.A., Andjelkovic, A.V., Kuziel, W.A., and Pachter, J.S. (2001). The chemokine receptor CCR2 mediates the binding and internalization of monocyte chemoattractant protein-1 along brain microvessels. J. Neurosci. *21*, 9214–9223.

Ginhoux, F., Greter, M., Leboeuf, M., Nandi, S., See, P., Gokhan, S., Mehler, M.F., Conway, S.J., Ng, L.G., Stanley, E.R., et al. (2010). Fate mapping analysis reveals that adult microglia derive from primitive macrophages. Science *330*, 841–845.

Gomez Perdiguero, E., Klapproth, K., Schulz, C., Busch, K., Azzoni, E., Crozet, L., Garner, H., Trouillet, C., de Bruijn, M.F., Geissmann, F., and Rodewald, H.R. (2015). Tissue-resident macrophages originate from yolk-sac-derived erythro-myeloid progenitors. Nature *518*, 547–551.

Gosselin, D., Link, V.M., Romanoski, C.E., Fonseca, G.J., Eichenfield, D.Z., Spann, N.J., Stender, J.D., Chun, H.B., Garner, H., Geissmann, F., and Glass, C.K. (2014). Environment drives selection and function of enhancers controlling tissue-specific macrophage identities. Cell *159*, 1327–1340.

Gosselin, D., Skola, D., Coufal, N.G., Holtman, I.R., Schlachetzki, J.C.M., Sajti, E., Jaeger, B.N., O'Connor, C., Fitzpatrick, C., Pasillas, M.P., et al. (2017). An environment-dependent transcriptional network specifies human microglia identity. Science *356*, 1–10.

Hagemeyer, N., Kierdorf, K., Frenzel, K., Xue, J., Ringelhan, M., Abdullah, Z., Godin, I., Wieghofer, P., Costa Jordão, M.J., Ulas, T., et al. (2016). Transcriptome-based profiling of yolk sac-derived macrophages reveals a role for Irf8 in macrophage maturation. EMBO J. *35*, 1730–1744.

Haynes, S.E., Hollopeter, G., Yang, G., Kurpius, D., Dailey, M.E., Gan, W.-B., and Julius, D. (2006). The P2Y12 receptor regulates microglial activation by extracellular nucleotides. Nat. Neurosci. *9*, 1512–1519.

Heng, T.S.P., and Painter, M.W.; Immunological Genome Project Consortium (2008). The Immunological Genome Project: networks of gene expression in immune cells. Nat. Immunol. *9*, 1091–1094.

Hickman, S.E., Kingery, N.D., Ohsumi, T.K., Borowsky, M.L., Wang, L.-C., Means, T.K., and El Khoury, J. (2013). The microglial sensome revealed by direct RNA sequencing. Nat. Neurosci. *16*, 1896–1905.

Hoeffel, G., Chen, J., Lavin, Y., Low, D., Almeida, F.F., See, P., Beaudin, A.E., Lum, J., Low, I., Forsberg, E.C., et al. (2015). C-Myb(+) erythro-myeloid progenitor-derived fetal monocytes give rise to adult tissue-resident macrophages. Immunity *42*, 665–678.

Hollingworth, P., Harold, D., Sims, R., Gerrish, A., Lambert, J.-C., Carrasquillo, M.M., Abraham, R., Hamshere, M.L., Pahwa, J.S., Moskvina, V., et al.; Alzheimer's Disease Neuroimaging Initiative; CHARGE consortium; EADI1 consortium (2011). Common variants at ABCA7, MS4A6A/MS4A4E, EPHA1, CD33 and CD2AP are associated with Alzheimer's disease. Nat. Genet. *43*, 429–435.

Huang, Y., Xu, Z., Xiong, S., Sun, F., Qin, G., Hu, G., Wang, J., Zhao, L., Liang, Y.-X., Wu, T., et al. (2018). Repopulated microglia are solely derived from the proliferation of residual microglia after acute depletion. Nat. Neurosci. *21*, 530–540.

Kierdorf, K., Erny, D., Goldmann, T., Sander, V., Schulz, C., Perdiguero, E.G., Wieghofer, P., Heinrich, A., Riemke, P., Hölscher, C., et al. (2013). Microglia emerge from erythromyeloid precursors via Pu.1- and Irf8-dependent pathways. Nat. Neurosci. *16*, 273–280.

Krasemann, S., Madore, C., Cialic, R., Baufeld, C., Calcagno, N., El Fatimy, R., Beckers, L., O'Loughlin, E., Xu, Y., Fanek, Z., et al. (2017). The TREM2-APOE pathway drives the transcriptional phenotype of dysfunctional microglia in neurodegenerative diseases. Immunity *47*, 566–581.e9.

Lavin, Y., Winter, D., Blecher-Gonen, R., David, E., Keren-Shaul, H., Merad, M., Jung, S., and Amit, I. (2014). Tissue-resident macrophage enhancer landscapes are shaped by the local microenvironment. Cell *159*, 1312–1326.

Li, Q., and Barres, B.A. (2018). Microglia and macrophages in brain homeostasis and disease. Nat. Rev. Immunol. *18*, 225–242.

Li, J., Chen, K., Zhu, L., and Pollard, J.W. (2006). Conditional deletion of the colony stimulating factor-1 receptor (c-fms proto-oncogene) in mice. Genesis *44*, 328–335.

Liddelow, S.A., Guttenplan, K.A., Clarke, L.E., Bennett, F.C., Bohlen, C.J., Schirmer, L., Bennett, M.L., Münch, A.E., Chung, W.-S., Peterson, T.C., et al. (2017). Neurotoxic reactive astrocytes are induced by activated microglia. Nature *541*, 481–487.

Mass, E., Ballesteros, I., Farlik, M., Halbritter, F., Günther, P., Crozet, L., Jacome-Galarza, C.E., Händler, K., Klughammer, J., Kobayashi, Y., et al. (2016). Specification of tissue-resident macrophages during organogenesis. Science *353*, aaf4238.

Matcovitch-Natan, O., Winter, D.R., Giladi, A., Vargas Aguilar, S., Spinrad, A., Sarrazin, S., Ben-Yehuda, H., David, E., Zelada González, F., Perrin, P., et al. (2016). Microglia development follows a stepwise program to regulate brain homeostasis. Science *353*, aad8670.

Metsalu, T., and Vilo, J. (2015). ClustVis: a web tool for visualizing clustering of multivariate data using principal component analysis and heatmap. Nucleic Acids Res. *43* (W1), W566–70.

Mildner, A., Schmidt, H., Nitsche, M., Merkler, D., Hanisch, U.-K., Mack, M., Heikenwalder, M., Brück, W., Priller, J., and Prinz, M. (2007). Microglia in the adult brain arise from Ly-6ChiCCR2+ monocytes only under defined host conditions. Nat. Neurosci. *10*, 1544–1553.

Obermeier, B., Daneman, R., and Ransohoff, R.M. (2013). Development, maintenance and disruption of the blood-brain barrier. Nat. Med. *19*, 1584–1596.

Ohgidani, M., Kato, T.A., Setoyama, D., Sagata, N., Hashimoto, R., Shigenobu, K., Yoshida, T., Hayakawa, K., Shimokawa, N., Miura, D., et al. (2014). Direct induction of ramified microglia-like cells from human monocytes: dynamic microglial dysfunction in Nasu-Hakola disease. Sci. Rep. *4*, 4957.

Priller, J., Flügel, A., Wehner, T., Boentert, M., Haas, C.A., Prinz, M., Fernández-Klett, F., Prass, K., Bechmann, I., de Boer, B.A., et al. (2001). Targeting gene-modified hematopoietic cells to the central nervous system: use of green fluorescent protein uncovers microglial engraftment. Nat. Med. *7*, 1356–1361.

Rathinam, C., Poueymirou, W.T., Rojas, J., Murphy, A.J., Valenzuela, D.M., Yancopoulos, G.D., Rongvaux, A., Eynon, E.E., Manz, M.G., and Flavell, R.A. (2011). Efficient differentiation and function of human macrophages in humanized CSF-1 mice. Blood *118*, 3119–3128.

Robinson, M.D., McCarthy, D.J., and Smyth, G.K. (2010). edgeR: a Bioconductor package for differential expression analysis of digital gene expression data. Bioinformatics *26*, 139–140.

Saederup, N., Cardona, A.E., Croft, K., Mizutani, M., Cotleur, A.C., Tsou, C.-L., Ransohoff, R.M., and Charo, I.F. (2010). Selective chemokine receptor usage by central nervous system myeloid cells in CCR2-red fluorescent protein knock-in mice. PLoS ONE *5*, e13693.

Sagar, D., Singh, N.P., Ginwala, R., Huang, X., Philip, R., Nagarkatti, M., Nagarkatti, P., Neumann, K., Ruland, J., Andrews, A.M., et al. (2017). Antibody blockade of CLEC12A delays EAE onset and attenuates disease severity by impairing myeloid cell CNS infiltration and restoring positive immunity. Sci. Rep. *7*, 2707.

Salter, M.W., and Stevens, B. (2017). Microglia emerge as central players in brain disease. Nat. Med. *23*, 1018–1027.

Schindelin, J., Arganda-Carreras, I., Frise, E., Kaynig, V., Longair, M., Pietzsch, T., Preibisch, S., Rueden, C., Saalfeld, S., Schmid, B., et al. (2012). Fiji: an open-source platform for biological-image analysis. Nat. Methods *9*, 676–682.

Schneider, C.A., Rasband, W.S., and Eliceiri, K.W. (2012). NIH Image to ImageJ: 25 years of image analysis. Nat. Methods *9*, 671–675.

Schulz, C., Gomez Perdiguero, E., Chorro, L., Szabo-Rogers, H., Cagnard, N., Kierdorf, K., Prinz, M., Wu, B., Jacobsen, S.E.W., Pollard, J.W., et al. (2012). A lineage of myeloid cells independent of Myb and hematopoietic stem cells. Science *336*, 86–90.

Scott, C.L., Zheng, F., De Baetselier, P., Martens, L., Saeys, Y., De Prijck, S., Lippens, S., Abels, C., Schoonooghe, S., Raes, G., et al. (2016). Bone marrow-derived monocytes give rise to self-renewing and fully differentiated Kupffer cells. Nat. Commun. *7*, 10321.

Sellgren, C.M., Sheridan, S.D., Gracias, J., Xuan, D., Fu, T., and Perlis, R.H. (2017). Patient-specific models of microglia-mediated engulfment of synapses and neural progenitors. Mol. Psychiatry *22*, 170–177.

Shi, Y., Yamada, K., Liddelow, S.A., Smith, S.T., Zhao, L., Luo, W., Tsai, R.M., Spina, S., Grinberg, L.T., Rojas, J.C., et al.; Alzheimer's Disease Neuroimaging Initiative (2017). ApoE4 markedly exacerbates tau-mediated neurodegeneration in a mouse model of tauopathy. Nature *549*, 523–527.

Subramanian, A., Tamayo, P., Mootha, V.K., Mukherjee, S., Ebert, B.L., Gillette, M.A., Paulovich, A., Pomeroy, S.L., Golub, T.R., Lander, E.S., and Mesirov, J.P. (2005). Gene set enrichment analysis: a knowledge-based approach for interpreting genome-wide expression profiles. Proc. Natl. Acad. Sci. USA *102*, 15545–15550.

Suzuki, R., and Shimodaira, H. (2014). pvclust: hierarchical clustering with p-values via multiscale Bootstrap resampling. R package version 1.2-2 https://cran.r-project.org/web/packages/pvclust/index.html.

Trapnell, C., Roberts, A., Goff, L., Pertea, G., Kim, D., Kelley, D.R., Pimentel, H., Salzberg, S.L., Rinn, J.L., and Pachter, L. (2012). Differential gene and transcript expression analysis of RNA-seq experiments with TopHat and Cufflinks. Nat. Protoc. *7*, 562–578.

van de Laar, L., Saelens, W., De Prijck, S., Martens, L., Scott, C.L., Van Isterdael, G., Hoffmann, E., Beyaert, R., Saeys, Y., Lambrecht, B.N., and Guilliams, M. (2016). Yolk sac macrophages, fetal liver, and adult monocytes can colonize an empty niche and develop into functional tissue-resident macrophages. Immunity *44*, 755–768.

Varvel, N.H., Grathwohl, S.A., Baumann, F., Liebig, C., Bosch, A., Brawek, B., Thal, D.R., Charo, I.F., Heppner, F.L., Aguzzi, A., et al. (2012). Microglial repopulation model reveals a robust homeostatic process for replacing CNS myeloid cells. Proc. Natl. Acad. Sci. USA *109*, 18150–18155.

Wang, Y., Cella, M., Mallinson, K., Ulrich, J.D., Young, K.L., Robinette, M.L., Gilfillan, S., Krishnan, G.M., Sudhakar, S., Zinselmeyer, B.H., et al. (2015). TREM2 lipid sensing sustains the microglial response in an Alzheimer's disease model. Cell *160*, 1061–1071.

Wong, K., Noubade, R., Manzanillo, P., Ota, N., Foreman, O., Hackney, J.A., Friedman, B.A., Pappu, R., Scearce-Levie, K., and Ouyang, W. (2017). Mice deficient in NRROS show abnormal microglial development and neurological disorders. Nat. Immunol. *18*, 633–641.

Zhang, Y., Chen, K., Sloan, S.A., Bennett, M.L., Scholze, A.R., O'Keeffe, S., Phatnani, H.P., Guarnieri, P., Caneda, C., Ruderisch, N., et al. (2014). An RNA-sequencing transcriptome and splicing database of glia, neurons, and vascular cells of the cerebral cortex. J. Neurosci. *34*, 11929–11947.

STAR★METHODS

KEY RESOURCES TABLE

REAGENT or RESOURCE	SOURCE	IDENTIFIER
Antibodies		
Donkey anti-rabbit BV421 IgG (1:300)	Biolegend	Cat# 406410; RRID: AB_10897810
Rat monoclonal anti-Mouse CD45 (1:200)	ebiosciences	Cat# 25-0451-82; RRID: AB_469625
Anti-CD11b microbeads	Miltenyi	Cat# 130-049-601
Rat anti-mouse Ly6g PercpCy5.5 (1:100)	Biolegend	Cat# 127615; RRID: AB_1877272
Rat anti-Mouse f4/80 APC (1:20)	Biorad	MCA497APC; RRID: AB_324435
PerCP/Cy5.5 anti-mouse/human CD45R/B220 (1:100)	Biolegend	Cat#103235; RRID: AB_893356
PE-Cy 7 mouse anti-Human CD45 (10μl/test)	BD Biosciences	Cat#557748; RRID: AB_396854
Anti-Mouse TMEM119 (0.25-0.5 μg/mL) Clone [28-3]	Abcam	Cat# 209064; RRID:AB_2728083
Rabbit anti-human TMEM119 (1:200)	Abcam	Cat# 185333; RRID: AB_2687894
PerCP/Cy5.5 anti-mouse/human CD11b (1:100-200)	Biolegend	Cat#101228; RRID: AB_893232
PerCP/Cy5.5 anti-mouse CD3 (1:100)	Biolegend	Cat#100217; RRID: AB_1595597
Human BD Fc Block (20 μl/300μl cells)	BD Biosciences	Cat#564220; RRID: AB_2728082
Brilliant Violet 421 goat anti-mouse IgG (1:250)	Biolegend	Cat#405317; RRID: AB_10900419
PerCP/Cy5.5 anti-mouse CD127(IL-7Ra) (1:100)	Biolegend	Cat#135021; RRID: AB_1937274
BV421 Goat anti-rabbit IgG polyclonal (1:300)	BD Biosciences	Cat#565014; RRID: AB_2716308)
PE anti-mouse CD117(c-kit) (1:200)	Biolegend	Cat#105807; RRID: AB_313216
Purified rat anti-mouse CD16/CD32 (10 μl/300μl stain)	BD Biosciences	Cat#553142; RRID: AB_394657
PerCP/Cy5.5 anti-mouse Ly-6G (1:100)	Biolegend	Cat#127615; RRID: AB_1877272
PerCP/Cy5.5 anti-mouse NK-1.1 (1:100)	Biolegend	Cat#108727; RRID: AB_2132706
Purified mouse IgG2b, k Isotype Ctrl (concentration matched to stain)	Biolegend	Cat#401201; RRID: AB_326631
Purified anti-human TMEM119 clone A16075D, (0.3 μg/ml)	Biolegend	Forthcoming
Goat anti-mouse/human IBA1 (1:500)	Abcam	Cat# 5076; RRID: AB_2224402
Anti-Human cytoplasm (2μg/mL)	Takara	Cat# Y40410; RRID: AB_2632385
Brilliant Violet 421 anti-mouse Ly-6C (1:100)	Biolegend	Cat#128031; RRID: AB_2562177
Rabbit polyclonal anti-Human Ms4a7 (1:30)	Atlas	Cat# HPA017418; RRID: AB_1854137
PE anti-mouse/human CD11b (1:100)	Biolegend	Cat#101207; RRID: AB_312790
PerCP/Cy5.5 anti-mouse/human CD11b (1:100)	Biolegend	Cat#101228; RRID: AB_893232
Anti-mouse CD45 PE-Cyanine7 (1:200)	eBioscience	Cat#25-0451-82; RRID: AB_469625
Goat anti-mouse IgG Alexa 647 (1:500)	Life Technologies	Cat#A21236; RRID: AB_2535805
Rat anti-mouse albumin (1:750)	Abcam	Cat#Ab24325; RRID: AB_448009
Biological Samples		
FVB Embryonic tissues	Charles River	Strain code: 207
Fetal brain tissue (human)	Stemexpress	N/A
Adult peripheral blood samples	Stanford Blood Center	N/A
Intraoperative brain tissue	Stanford Neurosurgery Tissue Bank	N/A
Post-mortem human brain samples	Stanford Brain Bank	N/A
Chemicals, Peptides, and Recombinant Proteins		
MS4A7 Peptide (40 molar excess)	Atlas	Cat# APrEST72174
TIC medium	Bohlen et al., 2017	N/A
Heat inactivated FCS	GIBCO	Cat#10437-028
ACK buffer	GIBCO	Cat#A10492-01

(*Continued on next page*)

Continued

REAGENT or RESOURCE	SOURCE	IDENTIFIER
RNAsin	Promega	Cat# N2615
DNaseI	Worthington	Cat# DPRFS
Trizol LS	Sigma	Cat# T3934
RLT buffer	QIAGEN	Cat# 79216
RLT Plus	QIAGEN	Cat# 1053393
DAB development Kit	Thermo Scientific	Cat# 34002
Z-4-Hydroxytamoxifen	Sigma-Aldrich	Cat# H7904
Human TGFβ2	Peprotech	Cat#100-35B
Human MCSF	Peprotech	Cat#300-25
Mouse MCSF	Peprotech	Cat#315-02
Ovine wool cholesterol	Avanti Polar Lipids	Cat# 700000P
LIVE/DEAD Green (1 μl/1ml cells)	Thermo Fisher	Cat# L34969
Critical Commercial Assays		
AllPrep Micro Kit	QIAGEN	Cat#80284
RNAeasy Micro Kit	QIAGEN	Cat# 74004
NEB Next Ultra RNaseq Kit	New England Biolabs	Cat# E7530S
RNAscope Fluorescent Multiplex Detection Reagents	ACDbio	Cat#320851
RNAscope Multiplex Fluorescent Detection Kit v2	ACDbio	Cat# 323110
RNAscope 2.5 HD Duplex Detection Reagents Kit	ACDbio	Cat# 322430
RNAscope H202 & Protease Plus Reagents	ACDbio	Cat#322330
RNAscope 2.5 Duplex Positive Control probe	ACDbio	Cat# 321641
TSA detection reagents; TSA plus Fluorescein	PerkinElmer	Cat# NEL741001KT
TSA detection reagents; TSA plus Cyanine 3	PerkinElmer	Cat# NEL744E001KT
TSA detection reagents; TSA plus Cyanine 5	PerkinElmer	Cat# NEL513001KT
Ovation-RNA-seq system V2	NuGEN	Cat# 7102
Probe: Hs-*TMEM119*	ACDbio	Cat# 478911
Probe: Mm-*Ms4a7*-C2	ACDbio	Cat#314601-C2
Probe: Mm-*Clec12a*-C2	ACDbio	Cat# 514351-C2
Probe: Hs-MS4A7	ACDbio	Cat# 514321
Probe: Mm-*Tmem119*-C2	ACDbio	Cat# 472901-C2
Probe: Mm-*Gpr56*	ACDbio	Cat# 318241
Bone marrow monocytes isolation kit	Miltenyi Biotec	Cat# 130-100-629
Deposited Data		
Microglia and MLC RNA-seq	This Paper	https://www.ncbi.nlm.nih.gov/bioproject/453419
Gene lists ALS UP, AD UP, LPS UP 1/2, DEV UP 1/2, CULTURE UP, and CULTURE DOWN	Figure 6 in Bohlen et al., 2017	N/A
Gene list SALL1 UP	(Buttgereit et al., 2016)	ArrayExpress: E-MTAB-5077
Gene list NRROS UP	(Wong et al., 2017)	https://www.nature.com/articles/ni.3743#supplementary-information
Mouse reference genome UCSC annotation mm9	UCSC Genome Browser	http://hgdownload.soe.ucsc.edu/downloads.html#mouse
Immune cell RNA-seq data	(Lavin et al., 2014; Zhang et al., 2014)	GEO: GSE63340; https://web.stanford.edu/group/barres_lab/brain_rnaseq.html
Experimental Models: Organisms/Strains		
Mouse: FVB.129X1-*Csf1r*^{tmErs} (also backcrossed to C57BL6 in this paper)	(Dai et al., 2002)/ Dr. Richard Stanley	RRID: MGI:3810944
Mouse: FVB/NCr	Charles River	RRID: MGI:2160605

(*Continued on next page*)

Continued

REAGENT or RESOURCE	SOURCE	IDENTIFIER
Mouse: C57BL/6-Tg (CAG-EGFP)131Osb/LeySopJ-	The Jackson Laboratory	RRID: IMSR_JAX:006567
Mouse: *Rag2*$^{tm1.1Flv}$ *CSF1*$^{tm1\ (CSF1)Flv}$ Il2rg$^{tm1.1FLv/J}$	The Jackson Laboratory	RRID: IMSR_JAX:017708
Mouse: *Rag2*$^{tm1.1Flv}$ *CSF1*$^{tm1\ (CSF1)Flv}$ *Il2rg*$^{tm1.1FLv/J}$ X *Csf1r*^{tmErs}	This paper	N/A
Mouse: *Cx3cr1*^{CreER}; B6	The Jackson Laboratory	RRID: IMSR_JAX:021160
Mouse: *Csf1r*^{flox}; B6	The Jackson Laboratory	RRID: IMSR_JAX: 021212
Mouse: *Cx3cr1*^{CreER};*Csf1r*^{flox} ; B6, *CXxcr1*^{CreER} mice were bred with Csf1r^{flox} mice	This paper	N/A
Mouse: Ccr2^{RFP}; B6	The Jackson Laboratory	RRID: IMSR_JAX: 017586
Mouse: C57BL6 WT	The Jackson Laboratory	RRID: IMSR_JAX:000664
Oligonucleotides		
Primers for Csf1r mice genotyping:		
F1; 5′-AGACTCATTCCAGAACCAGAGC-3′	This Paper	N/A
F2; 5′-CCGGTAGAATTCCTCGAGTCTA-3′	This Paper	N/A
R1; 5′-GAATTTGGAGTCCTCACCTTTG-3′	This Paper	N/A
Human *TMEM*119-6xhis Forward primer: 5′- AAAAGTCGACGCCGCCACCAtggtttcggcggcag 3′	This Paper	N/A
Human *TMEM*119-6xhis Reverse primer: 5′ -TTTTGCGGCCGCTTAGTGGTGATGGTGATG ATGACCAGAACCACCGACACTGGGGTGGAC ACTGC – 3′	This Paper	N/A
Human *TMEM*119-ECD Forward primer: 5′- AaaaaaggatccCgctctgtgcccctg –3′	This Paper	N/A
Human *TMEM*119-ECD Reverse primer: 5′ - TTT TTT TTG CGG CCG CCA TCA CGT ACT GGC –3′	This Paper	N/A
Software and Algorithms		
edgeR	(Robinson et al., 2010)	https://bioconductor.org/packages/release/bioc/html/edgeR.html
Tuxedo Pipeline	(Trapnell et al., 2012)	https://galaxyproject.org/
ICY	(de Chaumont et al., 2012)	http://icy.bioimageanalysis.org/
Graphpad Prism (version 7.0)	GraphPad	https://www.graphpad.com
Clustvis	(Metsalu et al., 2015)	https://biit.cs.ut.ee/clustvis_large/
Flowjo (version 10.4)	Treestar	https://www.flowjo.com
R (version 3.3.1)	The R foundation	https://www.r-project.org
Miseq	Illumina	N/A
JVenn	(Bardou et al., 2014)	http://jvenn.toulouse.inra.fr/app/example.html
Fiji	(Schindelin et al., 2012; Schneider et al., 2012)	https://imagej.net/Fiji
PVclust	(Suzuki and Shimodaira, 2014)	http://stat.sys.i.kyoto-u.ac.jp/prog/pvclust/
GSEA V3	(Subramanian et al., 2005)	http://software.broadinstitute.org/gsea/index.jsp
IPA	QIAGEN	https://www.qiagenbioinformatics.com/products/ingenuity-pathway-analysis
Other		
Dounce homogenizer, 7 ml	Wheaton	357542
Microcapillary tube	WPI	Cat#1B100f-4
DietGel Boost	ClearH20	Cat#72-04-5022

CONTACT FOR REAGENT AND RESOURCE SHARING

Further information and requests for resources and reagents should be directed to and will be fulfilled by the Lead Contact, F. Chris Bennett (eph.bennett@gmail.com).

EXPERIMENTAL MODEL AND SUBJECT DETAILS

Mouse Models

All animal studies were performed with approval from the Stanford Administrative panel on Laboratory Animal Care in accordance with institutional and national regulations. With the exception of humanized mice, all mice were immunocompetent. All mice appeared healthy, received regular monitoring from veterinary and animal care staff, and were not involved in prior procedures or testing. No animals used in this study experienced health morbidities. Animals were housed in a non-barrier facility with 12 hour light/dark cycles at 23+/−2°C, in disposable ventilated cages with no more than 5 animals per cage. Animals were provided water and standard chow *ad libitum*. Cages and bedding were changed every 2 weeks. *Csf1r* −/− pups, which lack teeth, were supplemented with DietGel Boost soft food (ClearH20), sometimes diluted with water, starting at p12. Immune compromised *Rag2*−/− *IL2rg*−/− *hMCSF*+/+ *Csf1r*−/− mice were provided irradiated food, but otherwise treated identically. We observed no evidence of infection or illness in these mice. No sentinel animals tested positive for infectious agents on any rack used in this study.

Csf1r −/− (FVB.129X1-Csf1r^{tm1Ers}) and *Csf1r* +/+ littermate animals on the FVB background were a generous gift from Dr. Richard Stanley, Albert Einstein College of Medicine, New York, USA. Adult WT FVB donor animals were bred from the identical starting strain. Timed FVB embryonic tissues were obtained from Charles River (Hollister, CA). For experiments using GFP-expressing donor cells, we backcrossed the *Csf1r* KO allele onto the C57BL/6 strain using MaxBax speed congenics (Charles River) for 5 generations to > 99.7% C57BL/6, then crossed 1 further generation. We generated a *Cx3Cr1*^{CreER}; *Csf1r*$^{fl/fl}$ line by intercrossing Jax 021212 and 021160. For experiments, we crossed *Cx3Cr1*^{CreER} +/−; *Csf1r*$^{fl/fl}$ to *Csf1r*$^{fl/fl}$ animals. To test whether engraftment required CCR2, we use *Ccr2* Rfp/Rfp homozygous donors (Jax 017586). We also used C57BL/6-Tg(CAG-EGFP)131Osb/LeySopJ ("Osb-GFP," Jax 006567) as a source for GFP-tagged donor cells. To generate the *Rag2*−/− *IL2rg*−/− *hMCSF*+/+ *Csf1r*−/− mouse we crossed the *Csf1r*^{tm1Ers} allele into C;129S4-*Rag2*$^{tm1.1Flv}$ *Csf1*$^{tm1(CSF1)Flv}$ *Il2rg*$^{tm1.1Flv/J}$ (Jax 017708). Animal lines were genotyped by Transnetyx (Cordova, TN) except pan-GFP animals which were genotyped by green florescence upon blue light exposure. We sometimes genotyped for Csf1r with in-house PCR (F1 5′-AGACTCATTCCAGAACCAGAGC-3′, F2 5′-CCGGTAGAATTCCTC GAGTCTA-3′, R1 5′-GAATTTGGAGTCCTCACCTTTG-3′). We verified *Csf1r* genotypes with second genotyping post-mortem. For all experiments, we used mixed sex donors and hosts at the specific fetal and adult developmental stages described in the method details below.

Human tissue samples

Human studies were approved by the Stanford Research Compliance Office and included IRB approval. Informed consent was obtained from all subjects. Postnatal brain macrophages used in transplantation experiments were obtained from n = 5 pediatric and adult neurosurgical resections for epilepsy (7 mo female, 3 yo female, 14 yo male, 28 yo female, 42 yo male), via the Stanford Neurosurgery Tissue Bank. We used pieces of cortex outside the epileptic focus; these were described as normal on MRI and by the operating surgeon. Fetal brain tissue (n = 2, 16-20 wk gestational age, biological sex could not be ascertained due to nature of clinical procedures preceding sample collection) was obtained from Stemexpress (Folsom, CA). Adult peripheral blood (n = 6) was obtained from the Stanford Blood Center (Palo Alto, CA). To protect personal information from healthy blood donors, we did not request information on sex nor age. All donor information was anonymized prior to investigator acquisition of samples. For human *in situ* hybridizations, flash frozen post-mortem brain tissue was obtained from the Stanford Brain Bank and diagnosed by E.P., a board-certified neuropathologist, thawed and fixed overnight in 4% PFA, then cryoprotected in 30% sucrose prior to frozen sectioning. We assessed N = 3 cases of severe AD pathology (80 yo male, 89 yo female also with diffuse Lewy Body disease, 79 yo female also with diffuse Lewy Body disease and cerebral amyloid angiopathy) and N = 1 case of severe cerebrovascular disease (85 yo male), comparing to N = 2 controls from temporal lobe epilepsy surgeries (49 yo male, 19 yo male).

METHOD DETAILS

General considerations for experimental design

Strategy for randomization and/or stratification

We performed no prospective treatment studies, and so did not have occasion to randomize a cohort to treatment arms. We performed all transplantation experiments identically, using all available *Csf1r* −/− hosts of age P0-4 on the day of donor tissue harvest. For BBB permeability stainings we included all animals of appropriate age on two separate days of harvest.

Blinding

Processing of RNaseq data, scoring of cell densities, percent TMEM119+ positive, and BBB integrity were performed blinded. RNaseq results were unblinded after mapping in order to group samples into donor cell types for subsequent analysis.

Sample-size estimations and method of computation

Sample-size estimations for RNaseq experiments were empirically based on past studies (Clarke et al., 2018; Zhang et al., 2014). For quantitative immunostaining experiments, we supplemented tissue from sequenced animals with littermates that we were not able to sort, or which did not yield adequate RNA for sequencing.

Inclusion and exclusion criteria of any data or subjects

For cell sorting, we included all surviving hosts for each transplantation experiment, and excluded animals that did not survive long enough to harvest. We excluded RNA samples from sorted cells when total yield was below the recommended input range for the Ovation V2 kit (Nugen), or when RIN was below 7 according to Bioanalyzer results (Agilent).

Microglia/MLC transplantation

For ICTs, P0-P4 *Csf1r* −/− pups and +/+ controls were injected as described previously (Bohlen et al., 2017) by hand using a pulled glass microcapillary tube in an electrode holder connected by silicon tubing to a syringe. One microliter containing a single cell suspension of donor cells in PBS was slowly injected bilaterally into cortex, 1-2 mm anterior and 2-3 mm lateral to lambda at a depth of 0.5-1 mm. Host animals were harvested after 14 days. Due to the constitutional fragility of *Csf1r* −/− animals, we harvested surviving animals of both sexes and pooled them for analyses. IP bone marrow injections were performed in P0-4 pups using an insulin syringe containing 20 μL of a single cell suspension in PBS. For adult CX3CR1-CreERT +/-;Csf1r fl/fl x Csf1r fl/fl ICTs, 5 month old mice were injected with 150mg/kg 4-hydroxy tamoxifen for two days. On day one, host animals were anesthetized with isofluorane, and five million bone marrow cells from Osb-GFP mouse donors were injected per hemisphere through two small burr holes bilaterally, approximately 1mm behind Bregma. The incision was closed using 4-0 vicryl sutures. Mice were treated with 5mg/kg subcutaneous carprofen analgesia and monitored closely post-operatively. Neonatal pups of CX3CR1-CreERT +/- ; Csf1r fl/fl x Csf1r fl/fl mice were injected daily between P1-P4 with 200mg/kg 4-hydroxytamoxifen subcutaneously. These hosts were then transplanted via direct intracerebral injection on day 5.

Donor tissue preparation

Microglia

Microglia were isolated as previously described (Bennett et al., 2016) with the following substitutions: Mice were euthanized by CO_2 asphyxiation and intravascularly perfused with 10 mL cold PBS, except for P5 animal brains which were carefully rinsed in PBS after dissection of the meninges. After myelin depletion using MACS beads, cell suspensions were positively selected for CD11b expression by magnetic bead separation using the MACS system (Miltenyi). Where applicable, mouse microglia were then cultured in TIC medium (described in Bohlen et al., 2017) supplemented with 10% heat inactivated FCS for 16-20 hours at 37°C and 10% CO_2, and subsequently harvested for RNA isolation or intracranial transplantation. Cells were cultured on tissue culture plastic, and harvested by incubation on ice for 5-10 minutes, followed by 3-5 washes with ice cold FACS buffer (PBS, 25 mM HEPES, 2mM EDTA, and 2% FCS) and repeated pipetting. 20-100 × 10^3 cells were injected per host based on cell yields. For injection of human brain macrophages, we used identical methods, except that for 2 of the adult brain samples we omitted CD11B+ selection due to limited sample size. For postnatal samples, we injected 2-40x10^3 cells, and for fetal, 5 × 10^3. Where applicable, we cultured human fetal brain macrophages identically to mouse, with the exception of using human MCSF (Peprotech) instead of mouse, at identical concentration.

Yolk sac

We manually dissected the yolk sac from 4-6 pregnant females at E8 (Charles River) into cold PBS (counting plug date as E0), yielding approximately 30 yolk sacs per prep. We then gently homogenized with 5 slow triturations each across successively smaller outlets (p1000 tip → p200 tip → 18 g needle → 27 g), and passed the homogenate over a 70 μm cell strainer. We next centrifuged for 5 min at 175 g, resuspended in 40 μL cold PBS, and injected 1 μL per pup (~0.75 yolk sacs per mice) into 30-40 pups across 5-7 litters.

Fetal brain

We manually dissected fetal brain tissue from E12-13 embryos into cold PBS, dissociated by 20 gentle triturations using a p1000 tip, and passed over a 40 μm cell strainer. To enrich for macrophages, we either used CD11B+ MACS positive selection as described for microglia or FACS, using the sort strategy shown in Figure S2B. We injected 2.5-8.5 × 10^3 cells per host as limited by cell yield.

Fetal liver

We manually dissected fetal liver from E13-14 embryos, homogenized by gentle trituration using a p1000, passed over a 40 μm strainer, and stained cells for FACS, using the sort strategy shown in Figure S2C. We injected 5-20 × 10^3 cells per host as limited by cell yield.

Bone marrow

We dissected femurs and tibia from 4-8 week old FVB WT, Osb-GFP and Ccr2 KO (Rfp/Rfp) animals of mixed sex, isolated whole bone marrow by flushing bones with PBS, and lysed RBCs using ACK as previously described (Bennett et al., 2016). For ICTs, we injected 100-200 × 10^3 cells per host. For IP BMTs we injected 2-5x10^6 cells per animal.

Bone marrow monocytes

We isolated bone marrow as described above, then enriched for bone marrow monocytes using the bone marrow monocyte isolation kit (Miltenyi), which enriches for monocytes by depletion of other cell types. We then stained this enriched population for

CD45, c-kit, Ly6c, NK1.1, CD3, B220, Il7ra, Siglecf, Ly6g using antibodies and dilutions shown in the key resources table, and sorted for monocytes using the sort strategy in Figure S3F. We injected 0.5-2 × 10^6 cells per mouse by the intraperitoneal route.

Blood

We collected whole blood from 6-8 week old FVB WT animals of mixed sex in 0.5M EDTA coated syringes by cardiac puncture, pooled blood from all animals in 0.05M final concentration of EDTA, and centrifuged at 1000 RPM for 12 minutes at RT. We then collected the buffy coat layer, lysed RBCs in 10-20 volumes ACK buffer (GIBCO) for 10 min at RT, centrifuged for 5 min at 200 g, washed x 1 and then resuspended in PBS. We injected 100-200 × 10^3 cells per host.

Flow cytometry

MG/MLC isolation

We generated single cell suspensions of MG/MLCs using dounce homogenization and MACS myelin depletion as described above, then followed methods described in Bennett et al. (2016). Briefly, we stained with a vital dye to exclude dead cells (Thermo Fisher), then for CD45, CD11b, and TMEM119 at dilutions shown in the Key Resources Table, adding RNAsin (Promega) and DNase (Worthington) to our sort tubes, following the sort strategy shown in Figure S1C.

Donor tissue isolation and analysis by FACS

For FACS sorting of donor tissues described above, we used identical staining protocols except performed centrifugation steps at 300 g for 5 minutes, and stained for different markers as described above. We performed all flow cytometry experiments using a large diameter (100 μm) nozzle at rates of 1-2.5 on BD FACSAria instruments in the Stanford Shared FACS Facility core. We sorted into FACS buffer for transplantation experiments. We used Flowjo software (Treestar) to analyze and visualize data. Gating strategies are shown wherever applicable in Figures S1, S2, and S7.

RNA and DNA extraction

We sorted engrafted cells directly into RNA extraction buffer. For BMT experiments we used Trizol LS (Sigma) according to manufacturer's protocols, collecting RNA and sometimes genomic DNA for genotyping of sorted cells. For one MG ICT experiment we sorted into RLT Plus (QIAGEN) and isolated both RNA and genomic DNA using the Allprep Micro kit. For remaining experiments we sorted into RLT buffer (QIAGEN) and isolated RNA using the RNAeasy micro kit with on column DNase digestion. We measured RNA quality by Agilent Bioanalyzer, and only processed samples with RIN > 7. We found that in order to reliably obtain adequate quantity and quality of RNA, we required 30 × 10^3 sorted cells.

RNaseq library construction and sequencing

We constructed and quality controlled libraries as described previously (Bennett et al., 2016), using the Nugen Ovation RNA-seq system V2, and the NEB Next Ultra RNaseq kit for Illumina, with 9-10 cycles of PCR enrightment. High quality libraries were sequenced by Miseq (Illumina), using 75 bp paired end reads. Aside from one WT control sample with 0.9x10^6, we obtained at least 1x10^6 paired reads per sample, with a range of 1-6x10^6. At least 70% of reads were mapped in all samples.

Anti-human Tmem119 antibody generation

To generate mouse anti-human TMEM119 FACS antibodies, we cloned the extracellular domain (ECD) after the signal peptide for human Tmem119 (corresponding residues: 26-95) into a custom pMAL vector for periplasmic MBP-ECD-8xHis fusion expression (gift from A. Ring, Yale University, New Haven, CT). We purified recombinant fusion proteins by Ni-NTA columns. BioLegend (San Diego, CA) immunized mice with the recombinant ECD proteins and screened positive multi-clone supernatants by ELISA. We tested multi- and then single-clone supernatants first by staining HEK cells transfected with His-tagged human Tmem119 expressed in pCMV-SPORT6 mammalian expression vector. For promising clones we verified that staining was blocked by pre-incubation with immunizing peptide, and tested them on primary human brain and blood tissue samples. We found that clone A16075D stained 70%–98% of CD45+/CD11B+ human brain cells with the highest signal to noise ratio; public release of clone A16075D by Biolegend is forthcoming.

Tissue Immunostaining

We performed immunostaining on 4% PFA perfusion- or immersion-fixed samples depending on whether whole animals or brain pieces were processed. Samples were cryoprotected in 30% sucrose-PBS, embedded in OCT (Fisher), cryosectioned (12-16 μm), mounted on Superfrost Plus slides (Fisher) and stored at −80° C until use. For mouse TMEM119 and IBA1 staining, we dried slides at 60°C, rehydrated in PBS, blocked for 1 hour at room temperature (RT) in PBSTx (PBS with 0.3%–0.5% Triton X-100) with 10% serum. We then incubated with primary antibodies in PBSTx/1% serum (staining buffer) overnight at 4°C. After washing, we incubated slides in staining buffer with Alexa-conjugated secondary antibodies (Life Technologies) for 2 hr at RT, then washed and coverslipped. Antibodies for MS4A7 (Atlas) and human TMEM119 (Abcam) required antigen retrieval prior to blocking. After rehydration, we boiled samples for 4 minutes in 10mM sodium citrate/0.05% Tween 20, pH 6, then incubated for 15 more minutes at RT in hot buffer. For MS4A7 peptide blocking studies, we obtained immunizing peptide from the antibody manufacturer (Atlas). We preincubated primary antibody with 40 molar excess of blocking peptide in 31.5 μL PBS overnight at 4°C prior to staining. To measure percent of parenchymal IBA1+ cells that were also TMEM119+, we provided numerically coded images obtained by FCB to FY, who also was not told the purpose of the experiment, but was instructed to mark all green cells (IBA1 channel), and then the

number of these that had any co-localized red (TMEM119 channel) staining. To measure cell density, we counted the number of nucleated TMEM119 positive cells in the same dataset, expressed as cells per unit area. To measure albumin and IgG accumulation in the brain parenchyma, we stained 30 micron sections from animals perfused at approximately 70% of cardiac output (0.07 x mass in grams) for albumin (Abcam) or IgG (Life Technologies), and compared to unstained tissue (IgG) or secondary only (albumin) controls processed in parallel for each sample. We examined all samples for qualitative evidence of local staining, and quantified mean florescence intensity in identical ROIs from the cortex. We expressed positive staining as a fold change over the MFI from negative control samples, propagating error accordingly.

RNA *in situ* hybridization

We performed *in situ* hybridizations on fixed frozen samples using the RNAscope system (ACDbio) with RNAscope 2.5 HD Duplex Reagent kit for colorimetric and Fluorescent Multiplex Reagent kit V2 for fluorescent development, according to manufacturer's protocols using TSA reagents (Perkin Elmer). When staining concurrently for IBA1 protein, we used our standard immunostaining protocol, omitting Triton-x100, with fluorescent secondary antibodies or HRP-conjugated secondary antibodies (Jackson Immuno-research) and DAB development kit (Thermo Scientific). Sections were counterstained with hematoxylin (colorimetric) or DAPI (fluorescent) for nuclei.

Image acquisition and processing

We acquired epifluorescence images using an Axio Imager M1 (Zeiss), except for stitched images in Figures 2, 3, and S2 for which we used a BZ-X700 Fluorescent Microscope (Keyence), confocal images for which we used an LSM710 (Zeiss) and DNA gels for which we used an Alpha Imager (Innotech). We acquired color images using an Axio Imager A2 (Zeiss). We analyzed images in Fiji (https://imagej.net/Fiji) or ICY (http://icy.bioimageanalysis.org), adjusting for brightness and black values (notes and raw images available upon request). We performed no other image math or processing.

Analysis of RNaseq data

We mapped, assembled transcripts, estimated FPKM, and analyzed differential gene expression as described previously (Bennett et al., 2016), using the tuxedo pipeline and edgeR, and identical reference genome. To avoid misinterpretation of expression differences in lowly expressed genes, we focused most analyses on genes with moderate or high expression in at least one cell type (FPKM > 20), and only interpreted gene expression differences with log2(FC)>1 and FDR < 0.05. To generate a correlation heatmap, we selected the top 1000 most variant genes across the datasets studied and used the R package gplots cor function to generate a map of Spearman coefficients for each comparison. When other published datasets were used, we normalized their reads to the average by a simple scalar. To make heatmaps, we used gplots heatmap.2 function. For PCAs, we used Clustvis. We ran analyses on the top 2500 most variant genes based on log2(FPKM+1 values), applying unit variance scaling to rows, and using SVD with imputation to calculate principal components. In PCA plots, ellipses predict cluster boundaries with probability 0.95. We used JVenn to create Venn diagrams showing shared and distinct differential gene expression. For hierarchical clustering and p value estimation, we used the pvclust package (Suzuki and Shimodaira, 2014). We clustered data based on Spearman correlation of the top 1000 most variant genes (using the unofficial version available at http://stat.sys.i.kyoto-u.ac.jp/prog/pvclust/), bootstrapping 10000x to arrive at the final p value. GSEA was performed using GSEA software V3, running 1000 permutations by phenotype, calculating weight enrichment and ranking genes by Signal2Noise. ALS UP, AD UP, LPS UP 1/2, DEV UP 1/2, CULTURE UP, and CULTURE DOWN were obtained from Bohlen et al. (2017). The Sall1 UP gene list represents the top 49 most upregulated genes in Sall1 KO microglia by fold change with FDR < 0.05 from Buttgereit et al. (2016). The NRROS UP gene list contains genes with log2 (NRROSKO/WT)>1.5 in sorted microglia/macrophages and adjusted p value < 0.05 from Wong et al. (2017). For the correlation plot in Figure 5B, we merged gene lists from *Sall−/−* microglia (log2(FC/WT)>1 or < -1) with those from HSC-MLCs, omitting genes for which edgeR was unable to obtain Log2FC values or did not appear in 1 of the 2 datasets. In Figure S5D, data were analyzed through the use of IPA (Qiagen).

Replicates

Number of biological replicates used in immunostaining and RNaseq experiments are specified below:

Adult microglia; Immunostaining: 6, RNaseq: 2
P5 microglia; Immunostaining: 5, RNaseq: 2
Cultured microglia; Immunostaining: 7, RNaseq: 4
Yolk sac; Immunostaining: 6, RNaseq: 3
Fetal Brain; Immunostaining: 3, RNaseq: 5
Bone marrow ICT; Immunostaining: 7, RNaseq: 7
Blood; Immunostaining; 9, RNaseq: 3
Bone marrow IP; Immunostaining; 9 RNaseq: 5
WT control; Immunostaining; 7, RNaseq: 7

QUANTIFICATION AND STATISTICAL ANALYSIS

To quantify gene expression from RNaseq data for comparison across samples (as shown in Figures 4G, 5C, 6A, S4A, and S5A–S5C; Tables S1–S5), we used FPKM values as generated by the Tuxedo pipeline. To measure relative gene expression between samples, we used Log2(fold change) as measured in edgeR (Figures 1C, 1D, 4D–4F, 5B, and S1G; Tables S1–S5, S6, and S7). We defined the statistical significance of differential gene expression between samples by false discovery rate (FDR) as calculated by edgeR, at a significance cutoff of 0.05 (Figures 1C, 1D, 4A, 4D–4G, 5C, 6A, S1G, and S5A–S5C; Tables S1–S5, S6, and S7). In some cases we also provided p values as reported by edgeR (Figures S2 and S3; Tables S6 and S7). We sometimes used FPKM cutoffs to focus analysis on genes of moderate or higher expression, as indicated in figure legends and results. To measure statistical significance of differences in macrophage density, we used Graphpad to perform either a Student's t test (unpaired, two tails; Figure S1B), applying Dunnett's test for multiple comparisons, or ANOVA (Figure S2E) with post hoc analysis of pairwise differences, adjusting for multiple comparisons. To quantify the correlation between *Sall1*−/− microglial and HSC-MLC gene expression, we performed linear regression in Graphpad and reported r and p values. To measure statistical significance of differences in average florescence intensity of IgG and Albumin stains (Figure S3C), we used Graphpad to perform Student's t tests (unpaired, two tails). All error bars (Figures 4G, 5C, 6A, S1B, S2E, S3C, and S5A–S5C) represent standard error of the mean, calculated either in Excel or Graphpad. To estimate statistical significance of hierarchical clustering branches shown in Figure 4C, we calculated p values using PVclust as described.

DATA AND SOFTWARE AVAILABILITY

All raw sequencing data are publicly available at National Center for Biotechnology Information (NCBI) BioProject, https://www.ncbi.nlm.nih.gov/bioproject. The accession number for the data reported in this paper is BioProject: PRJNA453419. Differential gene expression by EdgeR is available in Table S6. Mapped data (expressed as FPKM) and gene lists used in Figure 5 are available in Table S7.